Nonlinear dynamics of miniaturized dielectric elastomer actuators with surface effects

Akhil Pratap Singh[a], Gal Shmuel[b], Atul Kumar Sharma[a,*]

[a] *Soft Active Materials and Structures Laboratory, Department of Mechanical Engineering, Indian Institute of Technology Jodhpur 342030, India*

[b] *Faculty of Mechanical Engineering, Technion-Israel Institute of Technology, Haifa 32000, Israel*

Abstract

Dielectric elastomer actuators (DEAs) have attracted considerable attention for applications requiring lightweight, compliant, and large-strain electromechanical transduction. However, the reduction of operating voltage through miniaturization introduces pronounced surface and interfacial effects that can significantly alter the dynamic response and stability characteristics of these systems. In this work, a dynamic electromechanical framework is developed to investigate the nonlinear dynamics of miniaturized dielectric elastomer actuators while explicitly incorporating surface elasticity, intrinsic surface energy, and surface tension. The dielectric elastomer is modeled as an incompressible neo-Hookean ideal dielectric, and the governing nonlinear equation of motion is derived using an Euler-Lagrange formulation under finite deformation. An energy-based approach is further employed to predict the onset of dynamic pull-in instability and the associated critical conditions. The dynamic response under both DC and AC voltage excitations is examined through transient time-history analysis, phase portraits, Poincaré maps, and frequency-response characteristics. Particular attention is devoted to dynamic pull-in instability and its dependence on surface parameters. The predictions of critical instability parameters are verified through direct numerical integration of the nonlinear governing equation, showing close agreement. A comprehensive parametric study reveals how surface elasticity, intrinsic surface energy, and surface tension modify the effective stiffness, resonance behavior, and critical instability thresholds of miniaturized DEAs. The results demonstrate that surface effects substantially shift dynamic pull-in voltages and alter nonlinear oscillatory characteristics, highlighting their critical role in the design and development of miniaturized dielectric elastomer actuators operating under transient electromechanical loading.

Keywords: Miniaturized soft actuators, Dielectric elastomers, Surface effects, Nonlinear dynamics, Dynamic pull-in instability, Poincaré maps.

1. Introduction

Dielectric elastomers (DEs), a major class of smart electroactive polymers, are soft polymeric materials capable of undergoing large and reversible deformations when subjected to an electric field (Koh et al., 2010; Hajiesmaili

*Corresponding author

Email addresses: singh.107@iitj.ac.in (Akhil Pratap Singh), meshmuel@technion.ac.il (Gal Shmuel), atulksharma@iitj.ac.in (Atul Kumar Sharma)

& Clarke, 2021). Their low shear modulus, high dielectric breakdown strength, low mass density, and rapid electromechanical response enable actuation strains exceeding 100% under suitable loading and pre-stretch conditions (Pelrine et al., 2000; Zhao & Suo, 2010). A typical dielectric elastomer actuator (DEA) consists of a thin elastomeric membrane sandwiched between two compliant electrodes, forming a deformable parallel-plate capacitor. When a potential difference is applied, the resulting electric field generates Maxwell stresses that compress the membrane in the thickness direction and induce expansion in the in-plane directions (O'Halloran et al., 2008). The deformation is governed by the nonlinear coupling between finite elasticity and electrostatics, wherein the electric field modifies the mechanical stress state while the evolving geometry simultaneously alters the electric field distribution (Lu et al., 2020). Through this electromechanical coupling mechanism, DEs directly convert electrical energy into mechanical work with high energy density and large strain capability. These characteristics have led to extensive exploration of DEs in electromechanical transduction (Carpi et al., 2011; Hajiesmaili & Clarke, 2021), soft robotics (Guo et al., 2021; Li et al., 2025a), self-healing materials (Wang et al., 2023), micro-pumps (Pang et al., 2009; Eom et al., 2017), biomedical devices (Lu et al., 2016; Wang et al., 2022; Ghevondyan et al., 2025; Benouhiba et al., 2025), acoustics and vibration control (Zhao et al., 2016; Bortot & Shmuel, 2017; Sharma, 2020), tunable metamaterials (Yu et al., 2017; Shmuel, 2013; Zhu et al., 2018; Wang et al., 2020a; Sharma et al., 2022; Zhao et al., 2023), energy harvesting (Thomson et al., 2018; Gurjar et al., 2025), wearable electronics (Son et al., 2023), and micro air vehicles (Cao et al., 2019a), and many more.

In the context of continuum modeling of soft dielectric elastomer actuators operating in the dynamic regime, a large volume of literature has been devoted to elucidating their nonlinear time dependent response and the associated electromechanical instability phenomena (Zhu et al., 2010; Xu et al., 2012; Sheng et al., 2013, 2014; Dai & Wang, 2015; Joglekar, 2015; Zhu, 2015; Dai et al., 2016; Zhang et al., 2017; Sharma et al., 2018; Cao et al., 2019b; Sharma & Joglekar, 2019; Alibakhshi & Heidari, 2020; Wang et al., 2020b; Kashyap et al., 2020; Khurana et al., 2021a; Kumar et al., 2022; Xu et al., 2023; Cooley & Lowe, 2023; Alibakhshi et al., 2023; Ranjan et al., 2024; Pandey et al., 2024; Singh & Sharma, 2024; Wang et al., 2024; Guo et al., 2025; Zhang et al., 2025a; Guo et al., 2025). Among these studies, Zhu et al. (2010) established a nonlinear continuum-based dynamic framework for a pre-stretched circular dielectric elastomer membrane under coupled pressure and electrical loading, demonstrating that prestretch, applied pressure, and bias voltage strongly tune the natural frequencies, resonance behavior, and onset of instability, including harmonic, superharmonic, and subharmonic response branches. Xu et al. (2012) developed an analytical Euler-Lagrange framework for a homogeneously deforming sandwich type dielectric elastomer actuator, establishing the fundamental roles of oscillation, resonance, and damping in its nonlinear dynamic response. Sheng and co-workers (Sheng et al., 2013, 2014) developed thermodynamically consistent dynamic frameworks for dielectric elastomer membranes under coupled electromechanical loading, later extending them to include viscoelasticity and temperature effects, and demonstrated that prestress, damping, excitation frequency, and relaxation mechanisms strongly govern nonlinear oscillations, stability transitions, and hysteretic electromechanical behavior. In a series of studies, Joglekar and co-workers (Joglekar, 2014, 2015; Sharma et al., 2018; Sharma & Joglekar, 2019) developed energy-based frameworks for predicting DC dynamic pull-in instability in dielectric elastomer actuators, accounting for prestress, anisotropy, and actuator geometry, and showed that dy-

namic instability occurs at lower electric fields than the corresponding static thresholds while permitting larger admissible stretches prior to pull-in. Zhu (2015) further showed that under AC actuation, dynamic instability is governed by a frequency-dependent critical excitation amplitude with minimum thresholds near harmonic and subharmonic resonances, while prestretch significantly enhances the stability of the nonlinear response. Alibakhshi and co-workers (Alibakhshi & Heidari, 2020; Alibakhshi et al., 2023) showed that constitutive strain stiffening in dielectric elastomer balloons strongly influences snap-through thresholds, resonance characteristics, and chaotic oscillatory regimes under DC and combined DC-AC loading, with enhanced stiffening markedly improving dynamic stability. Ranjan et al. (2024) experimentally demonstrated that incorporating electrode mechanics into the dynamic modeling of dielectric elastomer actuators markedly alters equilibrium, resonance characteristics, and the onset of chaotic oscillations under time-varying electrical loading. Recent ANCF-based electromechanically coupled dynamic frameworks have further extended the modeling of dielectric elastomer actuators to complex geometries, multilayer architectures, and viscoelastic behavior, demonstrating the important roles of prestretch, viscoelasticity, and structural configuration in governing hysteresis, creep, voltage requirements, and frequency dependent nonlinear dynamics (Guo et al., 2025; Zhang et al., 2025a). Furthermore, a detailed review on nonlinear vibration analysis of soft DEAs was provided by Zhao et al. (2023). These studies have substantially advanced the current understanding of the nonlinear dynamic electromechanical response, resonance behavior, and instability mechanisms of DEAs, and have provided important guidelines for the design and optimization of DEAs under transient loading. However, these dynamic formulations are predominantly developed for macroscale systems and do not account for surface elasticity, intrinsic surface energy, and surface tension, whose influence becomes increasingly significant as the characteristic dimensions are reduced to the miniaturized scales.

Despite their significant advantages, the widespread deployment of DEs remains constrained by the high voltages required to achieve large actuation strains and the associated risk of electromechanical instability (EMI) (Zhao & Suo, 2007; Joglekar, 2014; Su et al., 2018; Dorfmann & Ogden, 2019; Yang & Sharma, 2023; Chen et al., 2024; Wu et al., 2025) and dielectric breakdown (Plante & Dubowsky, 2006; Suo, 2010; Godaba et al., 2019). In this context, several strategies have been proposed to reduce the operating voltage. One approach introduces mechanical anisotropy, for instance by embedding stiff fibers within the elastomer matrix to restrict deformation in selected directions and thereby promote enhanced unidirectional actuation at lower electric fields (Huang et al., 2004, 2012; Lu et al., 2012; Sharma & Joglekar, 2018; He et al., 2022). Mechanical anisotropy has also been achieved through electrode architecture, including the use of highly aligned carbon nanotube sheets to improve actuation efficiency (Cakmak et al., 2015). Another method involves incorporating high permittivity fillers into the polymer matrix to increase the effective dielectric constant and consequently lower the required voltage (Carpi & Rossi, 2005; Hossain, 2020; Asgari & Majidi, 2025). In recent years, alongside these material-level modifications, device miniaturization and multilayer stacking have emerged as particularly effective routes for voltage reduction, since the Maxwell stress scales with the square of the electric field and thinner membranes require smaller applied voltages to attain a given field intensity (Imamura et al., 2017; Zhou et al., 2021; Masud et al., 2022; Peng et al., 2024; Zhang et al., 2025b). However, as the membrane thickness approaches the micrometer scale, surface and interfacial effects become increasingly significant due to the elevated surface to volume ratio (Wang et al., 2021;

Lu et al., 2025; Li et al., 2025b). At such scales, electrode stiffness and thickness, interfacial adhesion in multilayer architectures, surface tension, and surface elasticity can substantially modify the electrically induced finite deformation response, alter the effective stiffness, and shift the critical thresholds for electromechanical and morphological instabilities in soft DEs (Wang & Zhao, 2013; Godaba et al., 2019; Zheng et al., 2021; Li et al., 2021; Rosales-Cuello et al., 2023; Liguori & Gei, 2023; Patra et al., 2024; Ranjan et al., 2024; Li et al., 2025b; Wu et al., 2025; Li et al., 2025b). Rosales-Cuello et al. (2023) experimentally demonstrated that increasing the electrode thickness in dielectric elastomer actuators leads to reduced deformation owing to the enhanced mechanical constraint imposed by the electrodes. Liguori & Gei (2023) employed an elastic surface-substrate interaction model to represent electrode stiffness as a boundary constraint and demonstrated its influence on the surface instabilities of dielectric elastomer membranes with surface elasticity under various actuation modes. Experimental studies on ultra-thin and multilayer DE structures (Ma et al., 2020; Duduta et al., 2016) have further shown that interfacial stresses and surface effects reduce actuation strain and shift instability thresholds. Furthermore, studies on morphological instabilities such as electro-creasing, wrinkling, and electro-cavitation in soft dielectrics (Wang & Zhao, 2013; Seifi & Park, 2017; Li et al., 2024; Seifi et al., 2016) indicate that surface-related effects become increasingly dominant when the electrocapillary length approaches the membrane thickness. Further, the miniaturized dielectric elastomer membranes are increasingly deployed in applications that inherently involve dynamic operation, including micro pumps (Lotz et al., 2010; Ghazali et al., 2017), soft robots (White, 2011; Ji et al., 2019), tactile and haptic interfaces (Matysek et al., 2010; Lotz et al., 2010), tunable acoustic absorber (Lu et al., 2017; Shrestha et al., 2024), micro resonators (Cao et al., 2019a; Alibakhshi et al., 2022), micro air vehicle (Cao et al., 2019a; Ji et al., 2019), etc. In such systems, time-dependent electrical excitation and oscillatory motion are intrinsic to the actuator functionality, and the transient electromechanical response governs both performance and stability. In particular, dynamic pull-in and morphological instabilities may occur at voltage levels that differ markedly from quasi static predictions (Joglekar, 2014; Godaba et al., 2017; Su et al., 2019; Liu et al., 2021), especially at small scales where surface effects are amplified. These considerations highlight the need for a dynamic modeling framework that explicitly incorporates surface elasticity, intrinsic surface energy, and surface tension, in order to quantify their influence on the nonlinear dynamic response and the critical thresholds at the onset of dynamic electro mechanical instability or pull-in instability in miniaturized dielectric elastomer actuators undergoing finite deformation.

Although the nonlinear dynamic behavior and electromechanical instability of dielectric elastomer actuators have been studied at macroscopic scales, a unified dynamic modeling framework that accounts for surface elasticity, intrinsic surface energy, surface tension, and equal biaxial prestress in dielectric elastomer actuators at miniaturized scales, in order to understand the coupled influence of prestress and surface effects on DC dynamic pull-in instability and the AC-driven nonlinear responses, remains lacking. This limitation hinders the design and development of dynamically stable miniaturized dielectric elastomer systems under transient loading. To address this gap, the present work reports a unified theoretical dynamic modeling framework, together with an energy-based formulation to predict the critical voltage and the associated thickness stretch at the onset of dynamic pull-in instability, explicitly accounting for all surface contributions and mechanical prestress. The analysis shows that surface effects increase the effective stiffness and shift the resonance branches toward higher frequencies. Fur-

thermore, surface elasticity introduces a critical threshold beyond which dynamic pull-in is entirely suppressed, whereas intrinsic surface energy and residual surface tension primarily elevate the critical instability voltage and thereby delay the onset of pull-in. A comprehensive study further reveals the role of mechanical prestress, together with surface-induced stiffening, on the stability of nonlinear vibrations in resonant, subharmonic, superharmonic, and near-resonant regimes. Notably, under a prescribed DC voltage, mechanical prestress enhances the actuation response by increasing the deformation level attained by the dielectric elastomer actuator. These findings establish a mechanistic basis for understanding how surface effects govern dynamic stability at miniaturized scales and provide a rigorous theoretical foundation for the design of dynamically robust dielectric elastomer-based devices.

The remaining paper is organized as follows. Section 2 presents a dynamic formulation for miniaturized dielectric elastomer actuators incorporating effects of surface elasticity, intrinsic surface energy, and surface tension, where in the problem description, finite deformation kinematics, and constitutive assumptions based on an incompressible neo-Hookean model of hyperelasticity coupled with ideal dielectric behavior are introduced, followed by the derivation of the nonlinear governing equation of motion via the Euler-Lagrange equation. Section 3 investigates the nonlinear dynamic response of the miniaturized dielectric elastomer actuator under both DC and AC voltage excitations, presenting the transient time history response, phase portraits, Poincaré maps, and frequency response curves to assess stability, periodicity, beating phenomena, and resonant behavior under harmonic loading, while the DC/Heaviside step voltage driven response is examined to determine dynamic pull-in instability thresholds, and a detailed parametric study is conducted to elucidate the effects of surface elasticity, intrinsic surface energy, surface tension, and equal biaxial pre-stress on the nonlinear dynamics and DC dynamic pull-in instability parameters, i.e., the critical stretch and applied voltage. Finally, Section 4 consolidates the key outcomes and discusses their implications for the design and development of miniaturized dielectric elastomer actuators operating under transient electromechanical loading.

2. Governing equations

This section reports the governing equations for exploring the dynamic electromechanical response of a soft dielectric elastomer actuator with surface effects. The problem description, kinematics, and constitutive model are first introduced, followed by the derivation of the equation of motion using an Euler-Lagrange formulation.

2.1. Problem definition, kinematics, and constitutive model

In this study, we consider an electrically driven unconstrained planar dielectric elastomer actuator, as shown in Fig. 1. The spatial and material coordinate systems are denoted by $[x_1, x_2, x_3]$ and $[X_1, X_2, X_3]$, respectively, and are assumed to coincide and centered at the mid-plane of the actuator. In the undeformed (reference) configuration, shown in Fig. 1(a), dielectric elastomer actuator of initial dimensions $L \times L \times H$ is sandwiched between two compliant electrodes and is free of external mechanical and electrical loads. In the deformed (current) configuration, shown in Fig. 1(b), the actuator is subjected to combined electrical and mechanical excitations consisting of an applied voltage $\phi(t)$ and equal biaxial in-plane forces of magnitude P. Consequently, the membrane deforms homogeneously such that its dimensions become $l = \lambda L$, and $h = \lambda_3 H$ along the planar directions, i.e., x_1 and x_2,

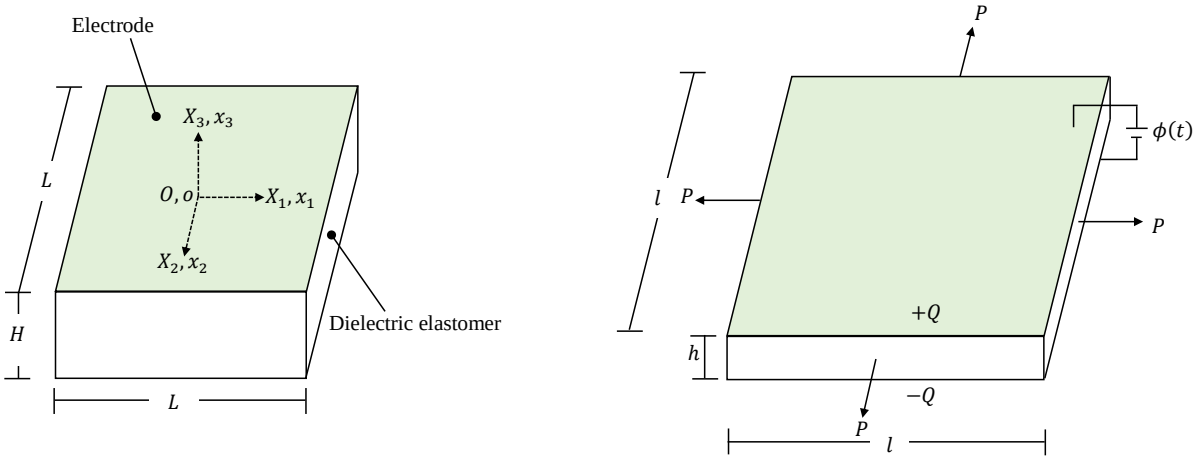

(a) (b)

Figure 1: Schematic of a dielectric elastomer actuator sandwiched between two compliant electrodes. (a) Reference configuration, in which the membrane is free of mechanical loads and electric excitation. (b) Deformed configuration, in which the membrane is subjected to equi-biaxial mechanical load P and a time-dependent electric potential $\phi(t)$.

and x_3 direction, respectively, while the compliant electrodes accumulate surface charges of $\pm Q$. The variables λ, and λ_3 denote the stretch ratios, which are assumed to be spatially uniform and functions of time only, i.e., $\lambda_i(t) =$ implying homogeneous deformation throughout the DEA. The dielectric elastomer is modeled as an isotropic and incompressible hyperelastic material, satisfying the constraint on volume change $l \times l \times h = L \times L \times H$. As a result of this constraint, the deformation can be fully characterized by the in-plane stretch ratio λ, while the thickness stretch follows as $\lambda_3 = \dfrac{1}{\lambda^2}$. Accordingly, the deformation mapping between the reference and current configurations of the actuator is described using the single independent stretch parameter λ as

$$x_1 = \lambda X_1; \quad x_2 = \lambda X_2; \quad x_3 = \frac{X_3}{\lambda^2}. \tag{1}$$

Therefore, the resulting homogeneous deformation gradient tensor $\mathbf{F}$ and the right Cauchy-Green deformation tensor $\mathbf{C}$ take the form

$$\mathbf{F} = \begin{bmatrix} \lambda & 0 & 0 \\ 0 & \lambda & 0 \\ 0 & 0 & \dfrac{1}{\lambda^2} \end{bmatrix}; \quad \mathbf{C} = \mathbf{F}^T\mathbf{F} = \begin{bmatrix} \lambda^2 & 0 & 0 \\ 0 & \lambda^2 & 0 \\ 0 & 0 & \dfrac{1}{\lambda^4} \end{bmatrix}. \tag{2}$$

To model the constitutive behavior of the dielectric elastomer, we adopt the ideal dielectric elastomer material model (Zhao & Suo, 2007), in which the total free energy density of the elastomer is expressed as

$$\Psi = \underbrace{\frac{\mu}{2}\left(\mathrm{tr}\,(\mathbf{C}) - 3\right)}_{\Psi^{\text{elastic}}} + \underbrace{\frac{\varepsilon}{2}E^2\lambda^4}_{\Psi^{\text{electrical}}}, \tag{3}$$

where Ψ^{elastic} represents the elastic contribution to the free energy density associated with the stretching of the dielectric elastomer, modeled using the incompressible neo-Hookean model of hyperelasticity, and $\Psi^{\text{electrical}}$ accounts for the electrical contribution for an ideal dielectric elastomer. The trace of the right Cauchy-Green deformation tensor is given by $\mathrm{tr}(\mathbf{C}) = 2\lambda^2 + \lambda^{-4}$, and the nominal electric field applied across the elastomer thickness is defined

as $E = \dfrac{\phi}{H}$. The material parameters μ and ε denote the shear modulus and dielectric permittivity of the elastomer, respectively.

It is well known that dielectric elastomer actuators in practical applications are often realized as ultra-thin, multilayered configurations, for which surface-related phenomena become very significant (Wang et al., 2021; Peng et al., 2024). In such miniaturized configurations of DEAs, the large surface area to volume ratio gives rise to additional energetic and mechanical contributions associated with intrinsic surface energy, surface tension, and surface elasticity (He & Park, 2018; Lu et al., 2025; Du et al., 2024). For capturing the electromechanical response and the onset of electro mechanical instability in miniaturized dielectric elastomers, it is therefore essential to explicitly incorporate these surface effects into the dynamic modeling framework. To account for these contributions, we consider the following surface constitutive model in which the surface energy per unit deformed area is defined as (Ru, 2010; Li et al., 2025b)

$$\Psi^{\text{surface}} = \gamma_s + \tau_s \left(\epsilon^s_{11} + \epsilon^s_{22}\right) + \frac{1}{2} E_s \left(\epsilon^s_{11} + \epsilon^s_{22}\right)^2, \tag{4}$$

in which γ_s denotes the surface energy density, i.e., the intrinsic energy stored per unit undeformed area of the dielectric elastomer; τ_s is the surface tension, characterizing the in-plane stress acting tangentially along the DE surface; E_s represents the surface elasticity, describing the elastic modulus of the surface layer/interface and contributes to the overall effective stiffness, without implying strain stiffening of the neo-Hookean bulk material; and $\epsilon^s_{11} = \dfrac{1}{2}(\lambda^2 - 1)$ and $\epsilon^s_{22} = \dfrac{1}{2}(\lambda^2 - 1)$ are the in-plane components of the surface strain tensor of the dielectric elastomer (He & Park, 2018).

In the following section, we devise the equation governing the nonlinear dynamic response of a planar dielectric elastomer actuator considering the surface effects.

2.2. *Dynamic equation of motion*

The equation of motion governing the nonlinear dynamics of the dielectric elastomer is obtained by invoking the Euler-Lagrange equation derived from the principle of least action, which is expressed as (Fox, 1987; Weaver Jr et al., 1991)

$$\frac{d}{dt}\left(\frac{\partial \mathcal{L}}{\partial \dot{q}}\right) - \frac{\partial \mathcal{L}}{\partial q} = 0, \tag{5}$$

where q and $\dot{q}$ denote the generalized coordinate of the system and its time derivative, which for the actuator considered here are taken as $q = \lambda$ and $\dot{q} = \dfrac{d\lambda}{dt}$. The quantity $\mathcal{L} = \mathcal{K} - \mathcal{U}$ represents the Lagrangian of the system, defined as the difference between the total kinetic energy $\mathcal{K}$ and the total potential energy $\mathcal{U}$ of the actuator.

The kinetic energy of the planar configuration of the dielectric elastomer actuator considered in the present study is obtained as (Xu et al., 2012)

$$\mathcal{K} = \frac{1}{2}\int_{x_1=-l/2}^{l/2}\int_{x_2=-l/2}^{l/2}\int_{x_3=-h/2}^{h/2} \rho\left(\dot{x}_1^2 + \dot{x}_2^2 + \dot{x}_3^2\right) \mathrm{d}x_1\, \mathrm{d}x_2\, \mathrm{d}x_3, \tag{6}$$

ρ denotes the mass density of the dielectric elastomer.

Assuming that the stretch ratio λ and its time derivative $\dot{\lambda}$ are spatially uniform and independent of the current configuration, and using Eq. (1), the kinetic energy of the actuator can be expressed in terms of the stretch ratio

and stretch rate as

$$\mathcal{K} = \frac{\rho H^3 L^2}{6}\frac{\dot{\lambda}^2}{\lambda^6} + \frac{\rho H L^4}{12}\dot{\lambda}^2. \tag{7}$$

For miniaturized DEAs, the thickness to lateral dimension ratio satisfies $H/L << 1$, such that the through thickness inertia term (first term in Eq. 7) is negligible relative to the in-plane inertia contribution (second term in Eq. 7).

The total elastic and electrostatic energy stored in the dielectric elastomer is obtained by integrating Eq. (3) over the entire deformed volume of the actuator, yielding

$$\mathcal{U}_{\text{electro-elastic}} = \frac{L^2 H}{2}\left[\mu\left(2\lambda^2 + \lambda^{-4} - 3\right) + \varepsilon\left(\frac{\phi}{H}\right)^2 \lambda^4\right]. \tag{8}$$

Under the assumption of homogeneous deformation and neglecting curvature effects, the total surface energy of the actuator, arising from the two planar free surfaces in the deformed configuration, is expressed using eq. (4) as

$$\mathcal{U}_{\text{surface}}(\lambda) = 2L^2\lambda^2\Psi^{\text{surface}} = 2L^2\lambda^2\left[\gamma_s + \tau_s\left(\lambda^2 - 1\right) + \frac{1}{2}E_s\left(\lambda^2 - 1\right)^2\right]. \tag{9}$$

As surface effects originate from deformation of the actuator induced by electro-mechanical loading, it is important to quantify the corresponding change in surface energy due to deformation, which is given, using Eq. (9), as

$$\Delta\mathcal{U}_{\text{surface}} = \mathcal{U}_{\text{surface}}(\lambda) - \mathcal{U}_{\text{surface}}(1) = 2L^2\left[\gamma_s\left(\lambda^2 - 1\right) + \tau_s\lambda^2\left(\lambda^2 - 1\right) + \frac{1}{2}E_s\lambda^2\left(\lambda^2 - 1\right)^2\right]. \tag{10}$$

The work done by the battery, corresponding to the change in the electrical potential of the power supply, is given by

$$\mathcal{U}_{\text{battery}} = -Q\phi = -L^2 H\varepsilon\left(\frac{\phi}{H}\right)^2 \lambda^4. \tag{11}$$

The work done by the applied in-plane equi-biaxial mechanical forces of magnitude P is given by

$$\mathcal{U}_{\text{mechanical}} = -2P(\lambda - 1). \tag{12}$$

Utilizing Eqs. (8)-(12), the total potential energy of the dielectric elastomer actuator is written as

$$\begin{aligned}\mathcal{U} &= \mathcal{U}_{\text{electro-elastic}} + \Delta\mathcal{U}_{\text{surface}} + \mathcal{U}_{\text{battery}} + \mathcal{U}_{\text{mechanical}} \\ &= \frac{L^2 H}{2}\left[\mu\left(2\lambda^2 + \lambda^{-4} - 3\right) - \varepsilon\left(\frac{\phi}{H}\right)^2 \lambda^4\right] \\ &\quad + 2L^2\left[\gamma_s\left(\lambda^2 - 1\right) + \tau_s\lambda^2\left(\lambda^2 - 1\right) + \frac{1}{2}E_s\lambda^2\left(\lambda^2 - 1\right)^2\right] - 2PL(\lambda - 1).\end{aligned} \tag{13}$$

Substituting the expressions for the total potential energy $\mathcal{U}$ and the kinetic energy $\mathcal{K}$ from Eqs. (13) and (7), respectively, into the Euler-Lagrange equation (5), the equation governing the nonlinear dynamics of the dielectric elastomer actuator, accounting for surface effects, takes the form

$$\begin{aligned}&\left(\frac{\rho L^4 H}{12} + \frac{\rho H^3 L^2}{6\lambda^6}\right)\frac{d^2\lambda}{dt^2} - \frac{\rho H^3 L^2}{2\lambda^7}\left(\frac{d\lambda}{dt}\right)^2 + \mu L^2 H\left(\lambda - \lambda^{-5}\right) - PL - \frac{\varepsilon L^2}{H}\phi^2\lambda^3 \\ &\quad + 2L^2\left[\gamma_s\lambda + \tau_s(2\lambda^3 - \lambda) + \frac{1}{2}E_s\lambda(\lambda^2 - 1)(3\lambda^2 - 1)\right] = 0.\end{aligned} \tag{14}$$

To elucidate the influence of surface energy density, surface elasticity, and surface tension on the dynamic response of dielectric elastomer actuators, both with and without mechanical pre-stress, we introduce the following set of non-dimensional variables and parameters:

$$\begin{aligned} \bar{t} &= t\sqrt{\frac{12\mu}{\rho H^2}}, \qquad c = \frac{L^2}{H^2}, \\ \bar{S} &= \frac{P}{\mu H L}, \qquad \bar{\phi} = \sqrt{\frac{\varepsilon}{\mu}}\frac{\phi}{H}, \\ \bar{\gamma}_s &= \frac{\gamma_s}{\mu H}, \qquad \bar{\tau}_s = \frac{\tau_s}{\mu H}, \qquad \bar{E}_s = \frac{E_s}{\mu H}. \end{aligned} \tag{15}$$

where $\bar{t}$ denotes the non-dimensional time, c is the non-dimensional geometric parameter, $\bar{S}$ represents the non-dimensional mechanical load, and $\bar{\phi}$ is the non-dimensional applied voltage. The parameters $\bar{\gamma}_s$, $\bar{\tau}_s$, and $\bar{E}_s$ are the non-dimensional quantities characterizing the effects of surface energy density, surface tension, and surface elasticity, respectively. Substituting these non-dimensional quantities from Eq. (15) into Eq. (14) yields the non-dimensional governing differential equation describing the dynamic motion of the actuator as

$$\begin{aligned} &\left(c + \frac{2}{\lambda^6}\right)\frac{d^2\lambda}{d\bar{t}^2} - \frac{6}{\lambda^7}\left(\frac{d\lambda}{d\bar{t}}\right)^2 + \left(\lambda - \lambda^{-5}\right) - \bar{S} - \bar{\phi}^2\lambda^3 \\ &\quad + 2\left[\bar{\gamma}_s\lambda + \bar{\tau}_s(2\lambda^3 - \lambda) + \frac{1}{2}\bar{E}_s\lambda(\lambda^2 - 1)(3\lambda^2 - 1)\right] = 0. \end{aligned} \tag{16}$$

In the present study, the actuator system is assumed to be initially at rest. Accordingly, the non-dimensional initial conditions are prescribed as

$$\lambda = 1, \qquad \text{and} \qquad \mathrm{d}\lambda/\mathrm{d}\bar{t} = 0, \tag{17}$$

where $\mathrm{d}(\cdot)/\mathrm{d}\bar{t}$ denotes differentiation with respect to the non-dimensional time.

The dynamic model of miniaturized DEAs derived in this section (Eq. 16) adopts the ideal dielectric assumption (Zhao & Suo, 2007; Lu et al., 2020), i.e., the permittivity is assumed to remain constant and independent of deformation or electric field. While this simplification allows us to isolate the influence of surface effects on the nonlinear dynamics and pull-in instability, it does not account for electrostriction, polarization saturation, or time-dependent dielectric relaxation effects (Jiménez & McMeeking, 2013; Saxena et al., 2014; Pelrine et al., 1998; Gei et al., 2014; Liu et al., 2015), which may become significant under high electric fields and in miniaturized DEAs. Furthermore, the present model neglects viscoelastic effects inherent to dielectric elastomers (Chiang Foo et al., 2012; Hossain et al., 2012). This assumption is generally reasonable for silicone-based elastomers (Yin et al., 2024; Guo et al., 2021; Madsen et al., 2016; Hu et al., 2022; Carpi et al., 2011), which exhibit relatively low viscoelastic losses. However, it may not be appropriate for acrylic elastomers (Hossain et al., 2012), where viscoelasticity is more pronounced and can significantly influence the dynamic response and pull-in instability thresholds.

In the following section, the nonlinear governing equation of motion for the actuator (Eq. 16) is solved numerically, together with the prescribed initial conditions (Eq. 17), using the built-in MATLAB solver `ODE45`. This numerical framework is employed to investigate the influence of surface related effects on the nonlinear dynamic response of a planar dielectric elastomer actuator. The `ODE45` algorithm is based on an explicit adaptive Runge-Kutta integration scheme of order 4(5), for which the local truncation error is of $O(\mathrm{d}\bar{t}^5)$, where $\mathrm{d}\bar{t}$ denotes the nondimensional time increment.

3. Results and discussion

This section demonstrates the capability of the proposed dynamic modeling framework by examining the influence of surface effects on the nonlinear dynamic behavior of miniaturized DEAs. Specifically, attention is focused on: (i) the dynamic response and electromechanical instability under DC (Heaviside type) voltage loading, and (ii) the dynamic response characteristics under harmonic (AC) voltage excitation.

For a miniaturized dielectric elastomer actuator composed of silicone-based soft elastomers, the bulk material parameters are taken as: shear modulus $\mu = 303$ kPa, density $\rho = 1100$ kg/m^3, and relative permittivity $\varepsilon_r = 2.8$ (Pelrine et al., 2000; Shi et al., 2022; Getz et al., 2017; Peng et al., 2024; Kornbluh et al., 2008; Lu et al., 2025). Representative surface parameters associated with surface-modified soft elastomers/interfaces are adopted as: surface energy density $\gamma_s = 0.02$ N/m, surface tension $\tau_s = 0.02$ N/m, and surface elasticity $E_s = 0.126$ N/m (Huang & Feng, 2008; Li et al., 2025b; Wang & Zhao, 2013; Lapinski et al., 2019; McCoul et al., 2017). For DEAs with thickness ranging from 1 μm to 10 μm, the corresponding nondimensional surface parameters span approximately $\bar{\gamma}_s \in (0.007, 0.1)$, $\bar{\tau}_s \in (0.007, 0.1)$, and $\bar{E}_s \in (0.04, 0.4)$.

In this study, to examine the influence of surface effects on the dynamic behavior of the DEA, three representative values of the nondimensional surface parameters are considered: $\bar{\gamma}_s = (0, 0.05, 0.1)$, $\bar{\tau}_s = (0, 0.05, 0.1)$, and $\bar{E}_s = (0, 0.2, 0.4)$. These values lie within the physically relevant ranges defined above. The case with $\bar{\gamma}_s = 0$, $\bar{\tau}_s = 0$, and $\bar{E}_s = 0$ corresponds to a dielectric elastomer without the effects of surface energy density, surface tension, and surface elasticity, respectively. Throughout this study, the nondimensional parameter c is set to 100.

3.1. Dynamic response and electromechanical instability under constant or DC voltage

In this section, the influence of surface effects on the nonlinear dynamic response and electromechanical instability of miniaturized DEAs subjected to DC voltage loading is examined for both equi-biaxially prestressed and without prestress configurations.

To understand the effects of surface energy density, surface tension, and surface elasticity on the DC dynamic response of the DEA, three representative values are considered for the corresponding nondimensional parameters: $\bar{\gamma}_s = (0, 0.05, 0.1)$, $\bar{\tau}_s = (0, 0.05, 0.1)$, and $\bar{E}_s = (0, 0.2, 0.4)$. In each case, the surface parameter of interest is varied while the remaining surface parameters are fixed at their respective reference values. Specifically, for the variation of surface energy density, $\bar{\tau}_s = 0.05$ and $\bar{E}_s = 0.2$ are prescribed; for the variation of surface tension, $\bar{\gamma}_s = 0.05$ and $\bar{E}_s = 0.2$ are fixed; and for the variation of surface elasticity, $\bar{\gamma}_s = 0.05$ and $\bar{\tau}_s = 0.05$ are maintained. The magnitude of the applied Heaviside step (constant) voltage is taken as $\bar{\phi} = 0.6$.

Figures 2(a) and 3(a) show the thickness-stretch time histories (λ_3 vs. $\bar{t}$) and the corresponding phase portraits ($d\lambda_3/d\bar{t}$ vs. λ_3) for the actuator without prestress ($\bar{S} = 0$) and with prestress ($\bar{S} = 0.5$), respectively, for the selected values of surface energy density. In both cases, the response remains periodic under DC loading. The deformation level ($1 - \lambda_3$), equivalently the oscillation amplitude, decreases monotonically with increasing surface energy density, indicating a pronounced surface-induced stiffening effect. Physically, increasing surface energy density elevates the surface free-energy contribution associated with deformation, thereby increasing the resistance of the elastomer to thickness contraction (Chen et al., 2022; Liu et al., 2014). Consequently, the effective stiffness of

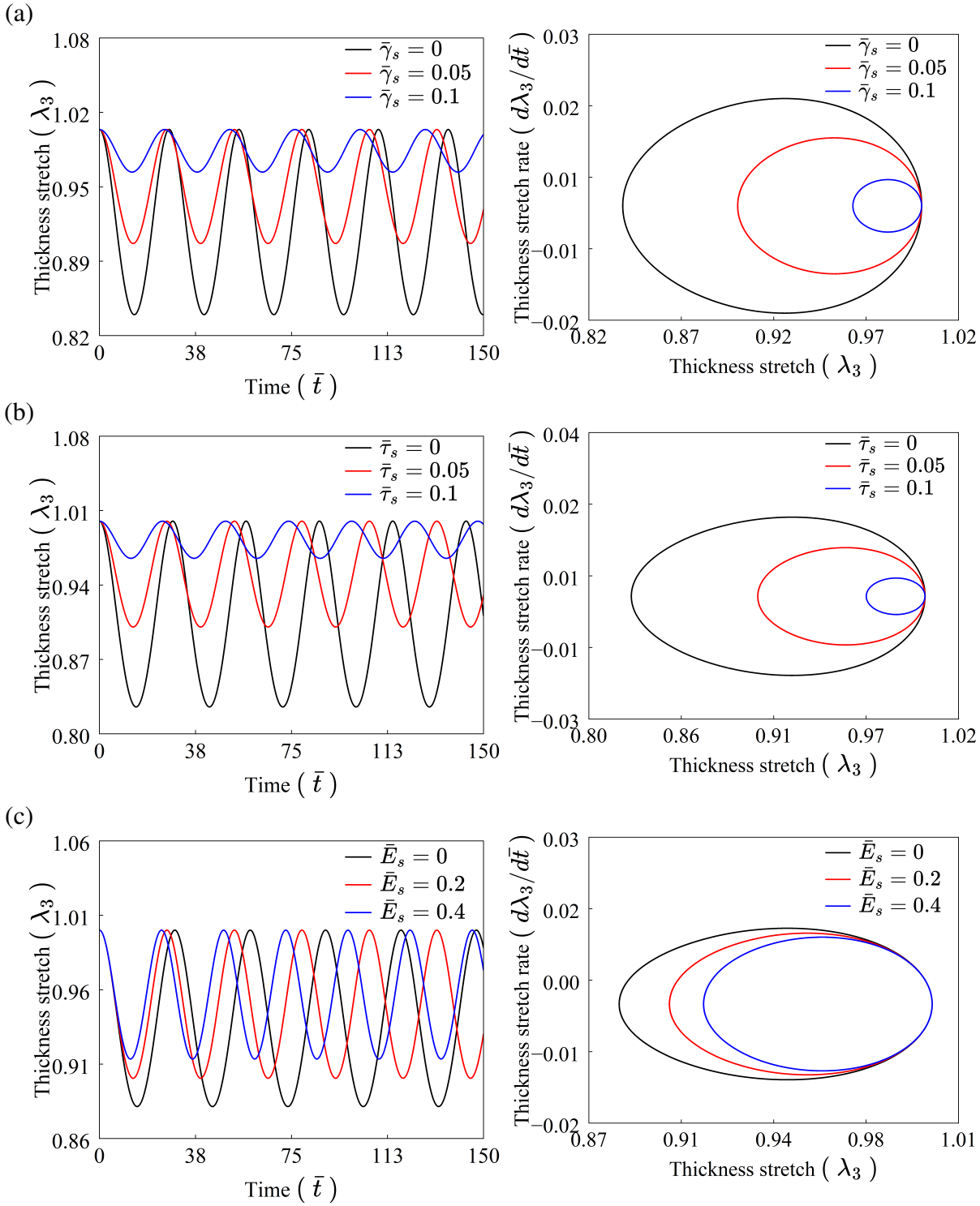

Figure 2: Effect of (a) surface energy density $\bar{\gamma}_s$, (b) surface tension $\bar{\tau}_s$, and (c) surface elasticity $\bar{E}_s$ on the nonlinear dynamic response of a dielectric elastomer actuator under DC voltage loading without prestress ($\bar{S} = 0$). The left and right panels correspond to the thickness-stretch time histories and the associated phase portraits, respectively.

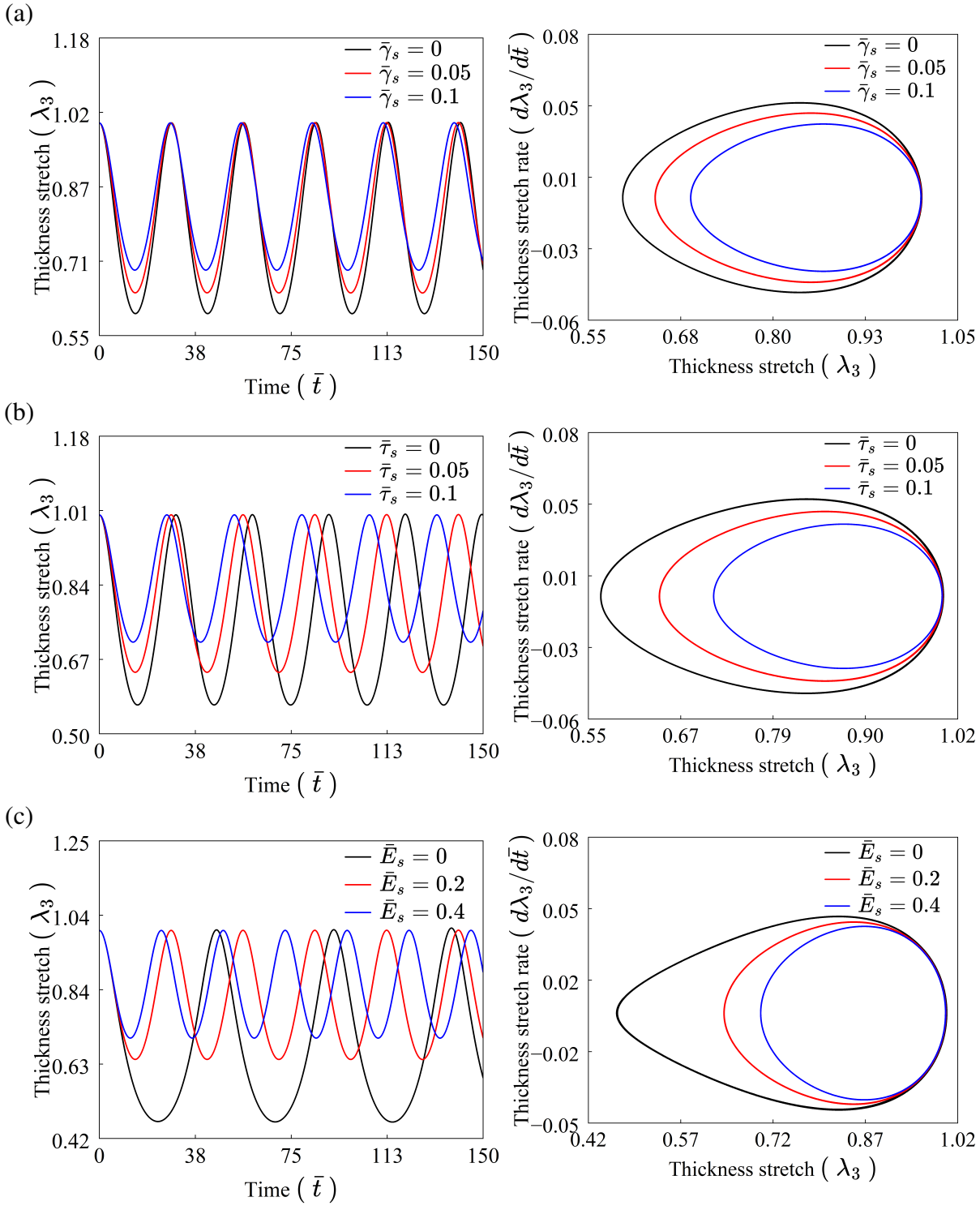

Figure 3: Effect of (a) surface energy density $\bar{\gamma}_s$, (b) surface tension $\bar{\tau}_s$, and (c) surface elasticity $\bar{E}_s$ on the nonlinear dynamic response of a dielectric elastomer actuator under DC voltage loading with prestress ($\bar{S} = 0.5$). The left and right panels correspond to the thickness-stretch time histories and the associated phase portraits, respectively.

the actuator increases, and a higher actuation voltage is required to attain a given oscillation amplitude. For all considered values of $\bar{\gamma}_s$, the prestressed actuator exhibits a larger deformation amplitude than the corresponding unstressed case, indicating that the combined action of mechanical prestress and electrical loading enhances thickness deformation and amplifies the dynamic response.

Figures 2(b) and 3(b) show the corresponding results for variations in surface tension. For both prestress levels, the response remains periodic under DC loading. As the surface tension parameter $\bar{\tau}_s$ increases, the thickness-stretch amplitude decreases, while the oscillation frequency undergoes a slight increase. This behavior is consistently reflected in the phase portraits, whose trajectories contract and become steeper with increasing $\bar{\tau}_s$. Physically, surface tension introduces an additional in-plane constraint that resists lateral expansion and, through incompressibility, suppresses thickness contraction (Seifi & Park, 2016). Consequently, the effective stiffness of the membrane increases, thereby limiting the growth of electrically induced deformation. This response highlights the underlying balance between prestress-assisted deformation and surface-tension-induced stiffening, which governs the DC electromechanical dynamics at miniaturized scales.

Figures 2(c) and 3(c) present the corresponding results for variations in surface elasticity. In all cases, the response remains periodic, while increasing $\bar{E}_s$ reduces the thickness-stretch amplitude and causes a slight increase in the oscillation frequency. The contraction of the phase trajectories with increasing surface elasticity signifies a reduction in the deformation level of the actuator. Physically, surface elasticity generates a strain-dependent surface stress that enhances the in-plane stiffness of the membrane (Style & Xu, 2018; Liu et al., 2014), thereby suppressing thickness contraction under electric loading. This stronger surface-induced stiffening is consistent with the later observation that sufficiently large surface elasticity can completely suppress dynamic pull-in instability.

Dielectric elastomer actuators are susceptible to electromechanical instability driven by the positive feedback between the applied electric field and membrane thinning (Zhao & Suo, 2007; Dorfmann & Ogden, 2019; Yang & Sharma, 2023). Next, we examine how surface parameters influence the onset of electromechanical instability in miniaturized DEAs subjected to DC dynamic loading. Following the energy-based approach proposed by Joglekar (2014), we formulate the Hamiltonian $\mathcal{H} = \mathcal{K} + \mathcal{U}$ of the DE actuator as

$$\begin{aligned}\mathcal{H} = {} & \frac{\rho H^3 L^2}{6}\frac{\dot{\lambda}^2}{\lambda^6} + \frac{\rho H L^4}{12}\dot{\lambda}^2 + \frac{L^2 H}{2}\left[\mu\left(2\lambda^2 + \lambda^{-4} - 3\right) - \varepsilon\left(\frac{\phi}{H}\right)^2 \lambda^4\right] \\ & + 2L^2\left[\gamma_s\left(\lambda^2 - 1\right) + \tau_s\lambda^2\left(\lambda^2 - 1\right) + \tfrac{1}{2}E_s\lambda^2\left(\lambda^2 - 1\right)^2\right] - 2PL(\lambda - 1)\end{aligned}. \tag{18}$$

As the considered miniaturized actuator system is conservative, the Hamiltonian $\mathcal{H}$ remains constant in time. Therefore, its value at the initial instant $t = 0$, when the actuator is at rest ($\lambda = 1$, $\dfrac{d\lambda}{dt} = 0$), is equal to its value at the instant of maximum overshoot within an oscillation cycle, $t = \tilde{t}$, where $\lambda = \lambda_m$ and $\dfrac{d\lambda}{dt} = 0$ (Sharma et al., 2018). Enforcing energy conservation between these two states yields

$$\begin{aligned}\mathcal{D} &= \mathcal{H}(\tilde{t}) - \mathcal{H}(0) \\ &= \left[\left(2\lambda_m^2 + \lambda_m^{-4} - 3\right) - \bar{\phi}^2\left(\lambda_m^4 - 1\right)\right] - 4\bar{S}(\lambda_m - 1) + 4\left[\bar{\gamma}_s(\lambda_m^2 - 1) + \bar{\tau}_s\lambda_m^2(\lambda_m^2 - 1) + \frac{1}{2}\bar{E}_s\lambda_m^2(\lambda_m^2 - 1)^2\right] = 0,\end{aligned} \tag{19}$$

which defines the stagnation curve relating the nondimensional voltage $\bar{\phi}$ to the corresponding maximum stretch λ_m attained during overshoot.

To determine the critical nondimensional voltage and the associated stretch at the onset of dynamic electromechanical instability, we impose the extremum condition $\frac{d\mathcal{D}}{d\lambda_m} = 0$, which leads to

$$\left(\lambda_m - \lambda_m^{-5}\right) - \bar{\phi}^2\lambda_m^3 - \bar{S} + \left[2\bar{\gamma}_s\lambda_m + 2\bar{\tau}_s\lambda_m(2\lambda_m^2 - 1) + \bar{E}_s\lambda_m(3\lambda_m^4 - 4\lambda_m^2 + 1)\right] = 0. \tag{20}$$

The simultaneous solution of the nonlinear algebraic equations (19) and (20) yields the critical nondimensional voltage, $\bar{\phi}^C$, and the corresponding critical thickness stretch, $\lambda^C = \frac{1}{\lambda_m^2}$, associated with the onset of dynamic electromechanical instability.

This energy-based approach of extracting the critical voltage and thickness stretch at the onset of dynamic pull-in instability relies on the static equilibrium states and is therefore computationally more efficient than direct numerical integration of the nonlinear equation of motion. This approach is motivated by the global bifurcation behavior of the system, wherein the transition from periodic to aperiodic motion occurs at the onset of dynamic instability. At this critical state, the actuator reaches a stagnation point characterized by vanishing velocity and

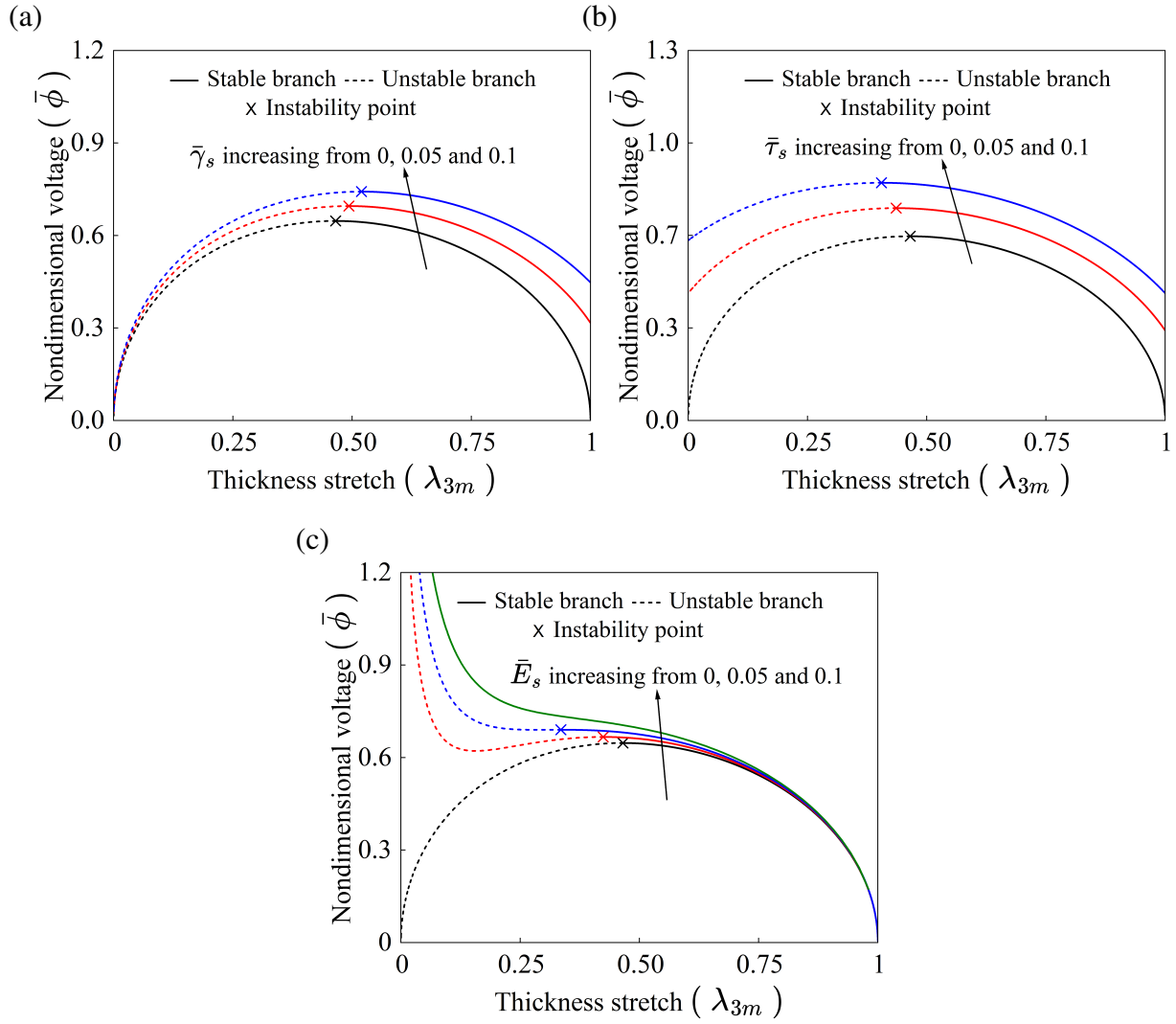

Figure 4: Variation of nondimensional voltage ($\bar{\phi}$) with thickness stretch (λ_{3m}) under DC voltage loading for different values of (a) surface energy density $\bar{\gamma}_s$, (b) surface tension $\bar{\tau}_s$, and (c) surface elasticity $\bar{E}_s$. Solid and dashed curves denote stable and unstable branches of the voltage-stretch response, respectively, while the × symbol indicates the onset of instability.

acceleration, corresponding to the maximum overshoot configuration and the softening induced by the nonlinear electrostatic force. Consequently, the system may be regarded as being in a pseudo-static equilibrium state at the onset of dynamic pull-in instability, thereby enabling the instability thresholds to be determined from static equilibrium conditions. Furthermore, a detailed discussion on the stagnation states associated with dynamic pull-in instability in dielectric elastomer actuators is presented in (Joglekar, 2014).

By numerically solving Eq. (19), the voltage-thickness stretch response ($\bar{\phi}$ vs. $\lambda_{3m} = 1/\lambda_m^2$) of the actuator is obtained for different values of the surface parameters $\bar{\gamma}_s$, $\bar{\tau}_s$, and $\bar{E}_s$. To assess the influence of surface energy density on the electromechanical instability, $\bar{\gamma}_s$ is varied while the other surface parameters are set to zero, i.e., $\bar{\tau}_s = \bar{E}_s = 0$. Likewise, the effects of surface tension and surface elasticity are examined independently by varying one parameter at a time while keeping the remaining two equal to zero. Figure 4(a) shows the influence of surface energy density on the voltage-stretch response, whereas Figs. 4(b) and 4(c) present the corresponding effects of surface tension and surface elasticity, respectively. The actuation curves comprise stable and unstable branches, indicated by solid and dashed lines. The stable branch represents periodic oscillatory motion, and the two branches

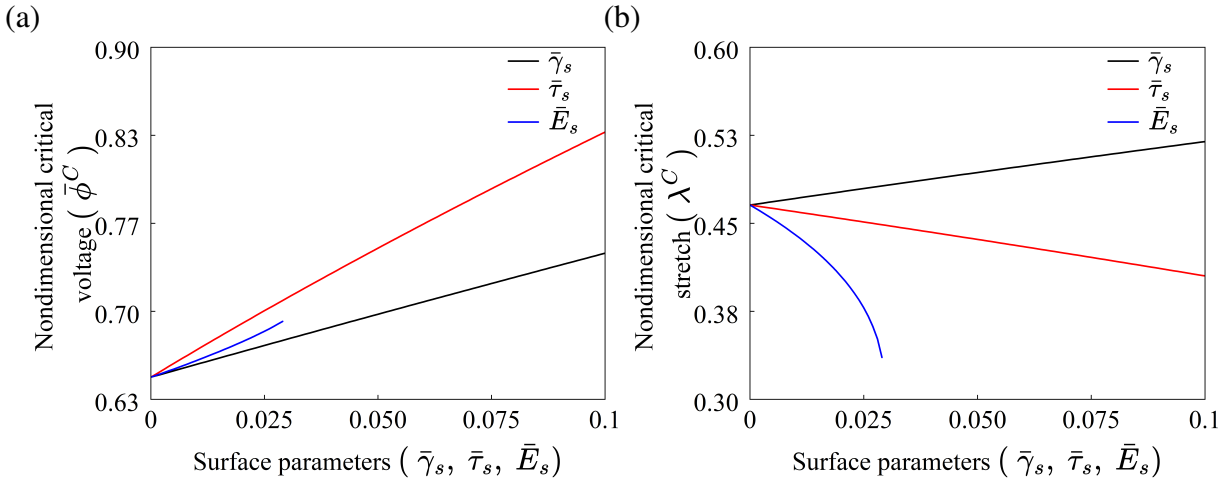

Figure 5: Variation of (a) nondimensional critical voltage ($\bar{\phi}^c$) and (b) critical thickness stretch (λ^c) with surface parameters under DC voltage loading. The plots illustrate the influence of surface energy density $\bar{\gamma}_s$, surface tension $\bar{\tau}_s$, and surface elasticity $\bar{E}_s$ on the onset of dynamic electromechanical instability of the DEA.

Surface energy density ($\bar{\gamma}_s$) ↓	Critical stretch (λ^c)	Critical voltage $\bar{\phi}^c$	Surface tension ($\bar{\tau}_s$) ↓	Critical stretch (λ^c)	Critical voltage $\bar{\phi}^c$	Surface elasticity ($\bar{E}_s$) ↓	Critical stretch (λ^c)	Critical voltage $\bar{\phi}^c$
0.00	0.4656	0.6470	0.00	0.4656	0.6470	0.00	0.4656	0.6470 (Joglekar, 2014)
0.025	0.4796	0.6713	0.025	0.4511	0.6980	0.007	0.4485	0.6557
0.05	0.4933	0.6953	0.05	0.4363	0.7459	0.015	0.4244	0.6666
0.075	0.5066	0.7188	0.075	0.4210	0.7915	0.021	0.4003	0.6756
0.10	0.5196	0.7421	0.10	0.4052	0.8350	0.029	0.3357	0.6899

Table 1: Variation of critical thickness stretch (λ^c) and nondimensional voltage ($\bar{\phi}^c$) at the onset of dynamic electromechanical instability under DC loading, for different values of surface energy density $\bar{\gamma}_s$, surface tension $\bar{\tau}_s$, and surface elasticity $\bar{E}_s$, in the absence of prestress ($\bar{S} = 0$). The case $\bar{\gamma}_s = \bar{\tau}_s = \bar{E}_s = 0$ corresponds to the classical response of an ideal DEA, and agrees well with previously reported results (Joglekar, 2014).

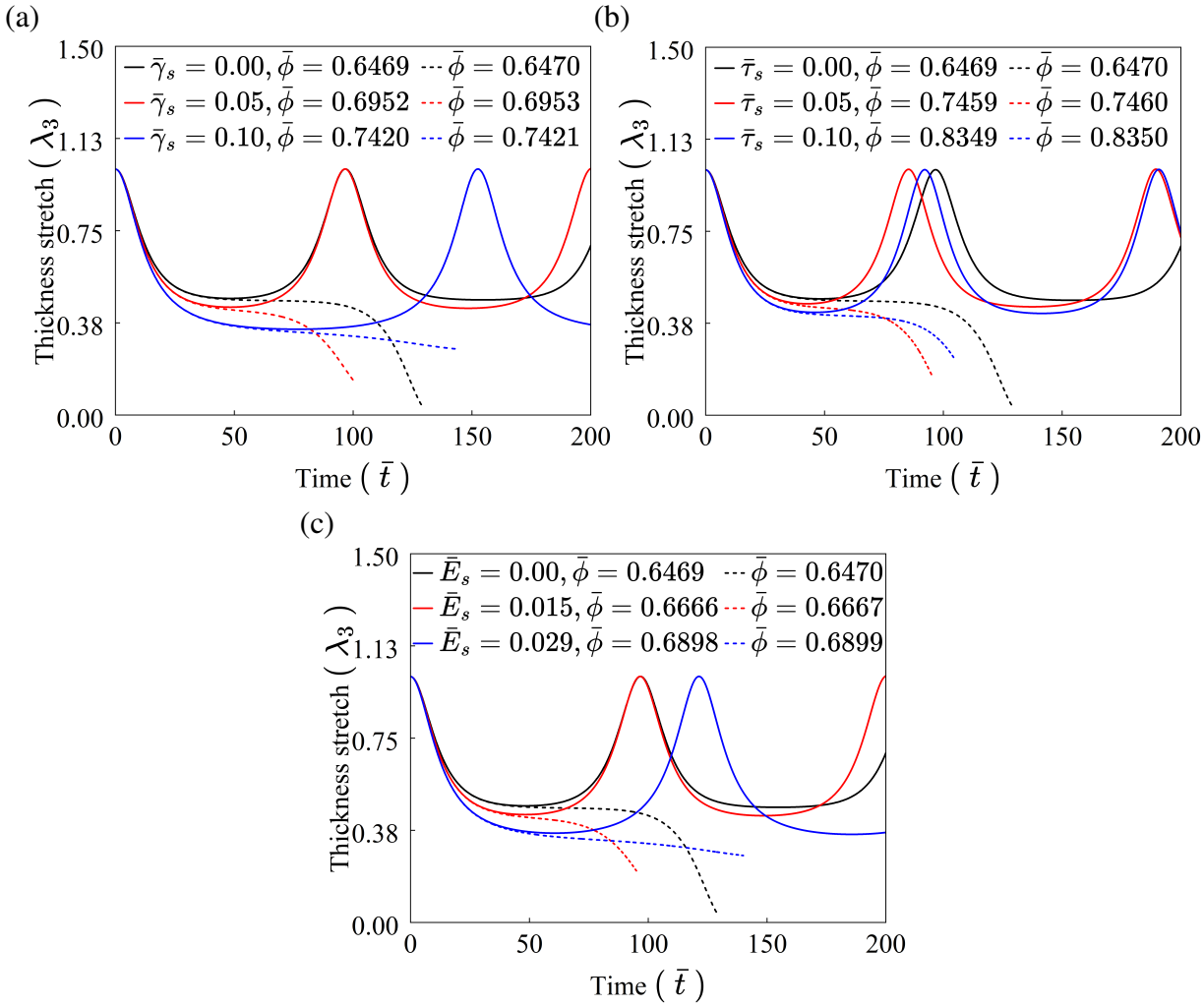

(c)

Figure 6: Nondimensional time-history responses of the actuator for two different values of the applied voltage, illustrating the transition from periodic to aperiodic oscillations near the onset of dynamic electromechanical instability under DC loading. Results are shown for different levels of (a) surface energy density $\bar{\gamma}_s$, (b) surface tension $\bar{\tau}_s$, and (c) surface elasticity $\bar{E}_s$.

merge at a saddle-node bifurcation point, marking the onset of electromechanical instability (denoted by the $\times$ symbol in Fig. 4). The deformation level $(1 - \lambda_{3m})$ at maximum overshoot, corresponding to the oscillation amplitude under DC dynamic loading, increases with increasing nondimensional voltage due to the enhanced Maxwell stress that promotes thickness contraction. From Fig. 4(c), it is further observed that beyond a critical value of surface elasticity, the electromechanical instability is completely suppressed. In particular, Eq. (20) indicates that instability is fully eliminated when $\bar{E}_s > 0.029$, leading to a monotonic voltage-stretch response and the disappearance of the bifurcation or electromechanical instability point. This indicates that surface elasticity may serve as a stabilizing design parameter. However, this stabilizing effect comes at the cost of reduced actuation deformation, so surface elasticity should be viewed as a design trade-off rather than an unqualified improvement. From a practical perspective, such level of surface elasticity can be engineered through electrode design (Liguori & Gei, 2023; Rosset & Shea, 2013), ultraviolet ozonolysis treatment (Lapinski et al., 2019), plasma treatment (Nemani et al.,

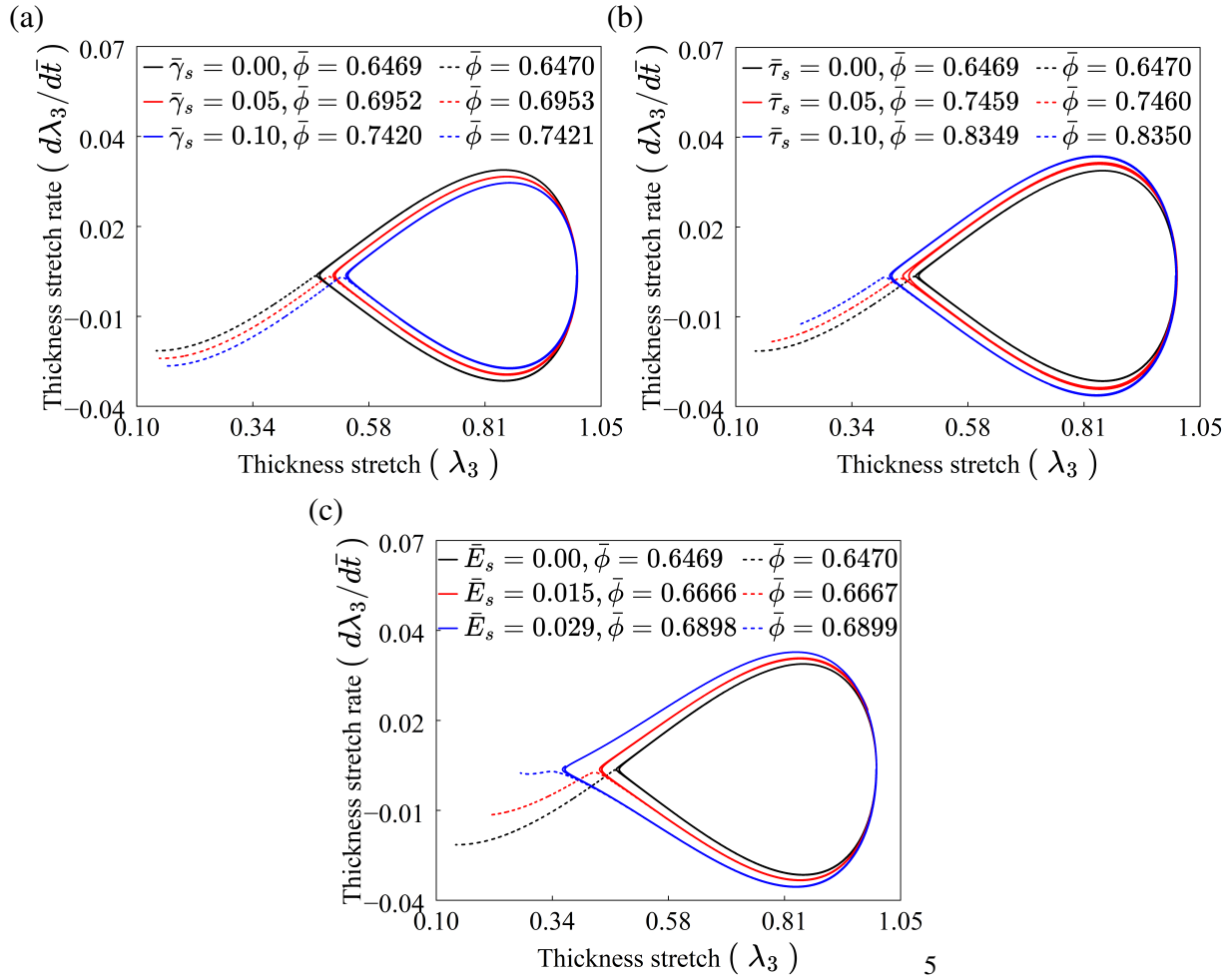

Figure 7: Phase portraits corresponding to the nondimensional time-history responses of the actuator shown in Fig. 7, illustrating the evolution of phase-space trajectories near the onset of dynamic electromechanical instability under DC loading. The transition from periodic to aperiodic motion is observed for two different values of the applied voltage. Results are presented for different levels of (a) surface energy density $\bar{\gamma}_s$, (b) surface tension $\bar{\tau}_s$, and (c) surface elasticity $\bar{E}_s$.

2018), or surface-modified elastomer layers (Mills et al., 2008), as reported in recent experimental studies.

The critical voltage and the associated thickness stretch at the onset of dynamic electromechanical instability, evaluated from Eqs. (19) and (20), are summarized in Table 1 for various surface parameter values and further depicted in Fig. 5. In the absence of surface effects, i.e., for $\bar{\gamma}_s = \bar{\tau}_s = \bar{E}_s = 0$, the present results reduce to the classical electromechanical response of an ideal DEA (Joglekar, 2014). The onset of electromechanical instability is predicted at a nondimensional voltage of approximately 0.6470, corresponding to a critical thickness stretch of 0.4656. These values are in close agreement with previously reported theoretical predictions (Joglekar, 2014), thereby verifying that the present formulation recovers the classical limiting case. Further, the results indicate that an increase in surface energy density shifts the instability point to higher voltages, accompanied by an increase in the critical thickness stretch (i.e., a reduced deformation level). This behavior arises from the additional surface energy contribution, which raises the overall energetic barrier and necessitates a stronger electric field to initiate instability. In contrast, increasing surface tension or surface elasticity also elevates the critical voltage, but

reduces the critical thickness stretch (i.e., increases the deformation level at instability), thereby promoting greater thickness contraction once the instability condition is attained. These surface effects augment the effective in-plane stiffness of the membrane, which postpones the onset of instability and enhances stability under substantial electric loading. Consequently, surface tension and surface elasticity expand the attainable actuation range while maintaining a stable electromechanical response.

The critical voltage and the associated thickness stretch at the onset of dynamic instability, predicted by the foregoing energy-based formulation, are further verified through direct numerical integration of the nonlinear equation of motion given in Eq. (16). For various levels of surface energy density ($\bar{\gamma}_s$), surface tension ($\bar{\tau}_s$), and surface elasticity ($\bar{E}_s$) listed in Table 1, the time-history responses and corresponding phase portraits are presented in Figs. 6 and . 7, respectively, to identify the transition from periodic to aperiodic motion. When the applied voltage is below the predicted critical value, the actuator exhibits sustained periodic oscillations characterized by closed phase trajectories. As the voltage approaches the critical level for a given set of surface parameters, the oscillation period increases significantly, and at the instability point the system reaches a stagnation state with an unbounded period, indicating a saddle-node bifurcation. Beyond this threshold, the response becomes aperiodic and the phase trajectories open, signifying loss of dynamic stability. An iterative procedure based on assessing the periodicity of the time-history response is employed to extract the instability parameters. With increasing surface tension or surface elasticity, the periodic orbits persist up to higher voltage levels, demonstrating the stabilizing influence of surface effects. The critical stretches and nondimensional voltages obtained from the time-domain simulations are in close agreement with those predicted by the energy-based approach for all considered surface parameter values.

3.2. Dynamic response under harmonic (AC) voltage excitation

This section investigates the influence of surface effects on the nonlinear dynamic response of miniaturized dielectric elastomer actuators subjected to harmonic voltage excitation. The applied voltage is prescribed in nondimensional form as (Zhu, 2015)

$$\bar{\phi} = \bar{\phi}_a \sin(\bar{\omega}\,\bar{t})\,, \tag{21}$$

where $\bar{\phi}_a$ denotes the amplitude of the applied nondimensional voltage and $\bar{\omega}$ is the nondimensional angular excitation frequency. In the present study, the voltage amplitude is fixed at $\bar{\phi}_a = 0.3$. To elucidate the role of surface energy density, surface tension, and surface elasticity on the forced response characteristics, the frequency-response curves, time-history plots, phase portraits, and Poincaré maps are evaluated for representative values of the surface parameters.

We first investigate the influence of surface energy density $\bar{\gamma}_s$, surface tension $\bar{\tau}_s$, and surface elasticity $\bar{E}_s$ on the frequency-response characteristics of the actuator. Figure 8 shows the variation of the oscillation amplitude λ_3^a with the nondimensional excitation frequency $\bar{\omega}$ for DEA without prestress ($\bar{S} = 0$) and with prestress ($\bar{S} = 0.5$) configurations, considering the same three representative values of $\bar{\gamma}_s$, $\bar{\tau}_s$, and $\bar{E}_s$ introduced in the preceding DC dynamic analysis. Here, the oscillation amplitude is defined as $\lambda_3^a = \dfrac{\lambda_3^{\max} - \lambda_3^{\min}}{2}$, where $\lambda_3^{\max}$ and $\lambda_3^{\min}$ denote the maximum and minimum values of the thickness stretch attained during oscillation, respectively.

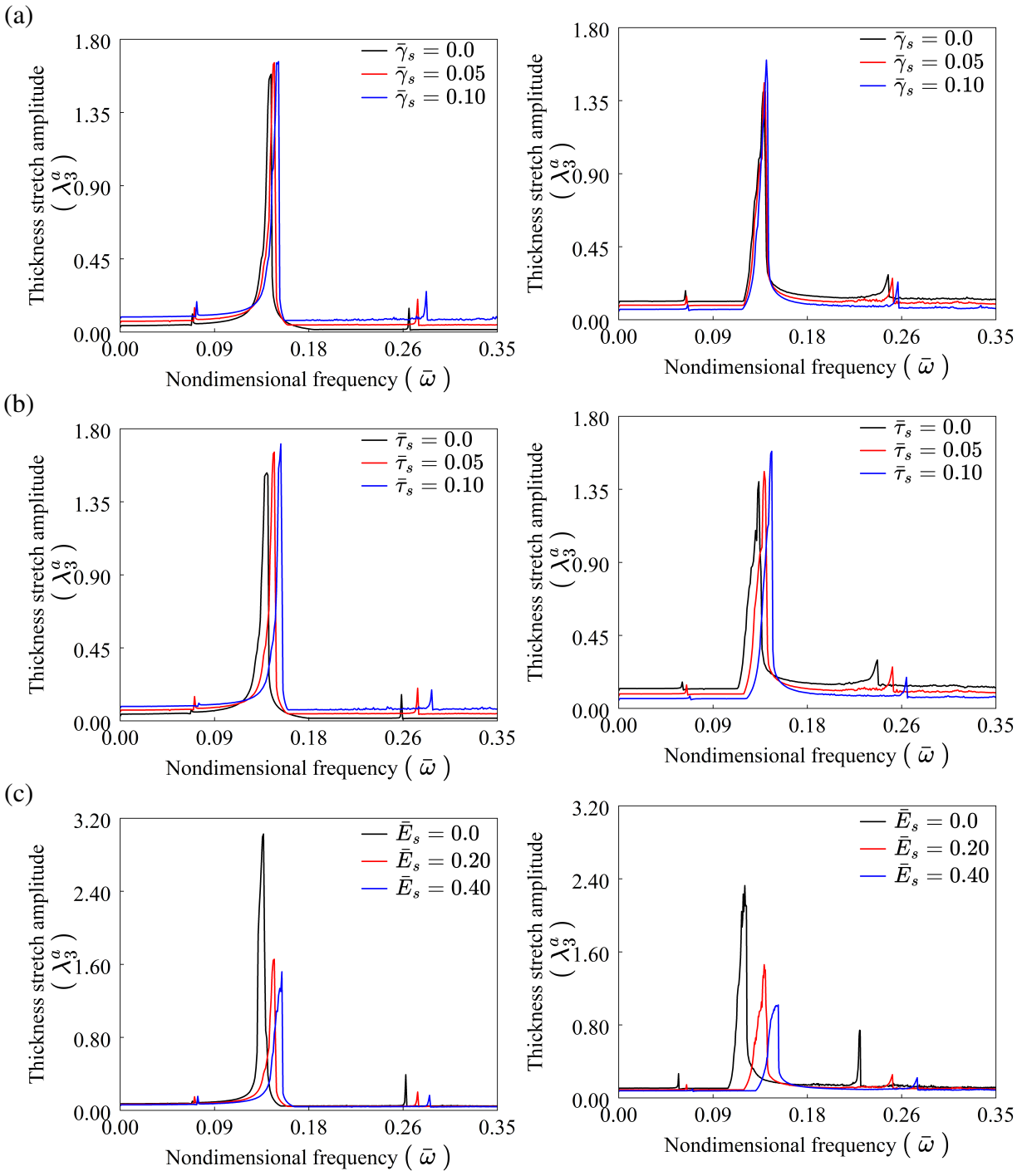

Figure 8: Effect of (a) surface energy density $\bar{\gamma}_s$, (b) surface tension $\bar{\tau}_s$, and (c) surface elasticity $\bar{E}_s$ on the frequency-amplitude response of a dielectric elastomer actuator without prestress ($\bar{S} = 0$) and with prestress ($\bar{S} = 0.5$), shown in the left and right panels, respectively.

The frequency-response characteristics exhibit three distinct resonance branches associated with subharmonic ($\bar{\omega} < \bar{\omega}_0$), primary (harmonic), and superharmonic ($\bar{\omega} > \bar{\omega}_0$) excitations (Zhu, 2015; Nayfeh & Mook, 2024; Khurana et al., 2021b). The branch attaining the maximum oscillation amplitude λ_3^a defines the fundamental resonance frequency $\bar{\omega}_0$ of the miniaturized DEA. For all three surface effects, namely surface energy density, surface tension, and surface elasticity, the resonance frequencies undergo a upward shift with increasing surface contribution, indicating an increase in the effective stiffness of the electromechanical system. This surface-induced stiffening is observed consistently for both the cases of DEA with and without prestress, as summarized in Tables 2-4. Among

Surface Energy Density ($\bar{\gamma}_s$) ↓	Normalized Harmonic Resonance Frequency ($\bar{\omega}_0$)		Normalized Subharmonic Resonance Frequency		Normalized Superharmonic Resonance Frequency	
	$\bar{S} = 0$	$\bar{S} = 0.5$	$\bar{S} = 0$	$\bar{S} = 0.5$	$\bar{S} = 0$	$\bar{S} = 0.5$
0	0.1402	0.1343	0.0670	0.0622	0.2683	0.2506
0.05	0.1433	0.1350	0.0692	0.0630	0.2762	0.2545
0.1	0.1471	0.1372	0.0708	0.0641	0.2841	0.2591

Table 2: Normalized resonance frequencies corresponding to harmonic ($\bar{\omega}_0$), subharmonic, and superharmonic resonance excitation regimes for different values of surface energy density $\bar{\gamma}_s$, for both without prestress ($\bar{S} = 0$) and prestressed ($\bar{S} = 0.5$) configurations.

Surface Tension ($\bar{\tau}_s$) ↓	Normalized Harmonic Resonance Frequency ($\bar{\omega}_0$)		Normalized Subharmonic Resonance Frequency		Normalized Superharmonic Resonance Frequency	
	$\bar{S} = 0$	$\bar{S} = 0.5$	$\bar{S} = 0$	$\bar{S} = 0.5$	$\bar{S} = 0$	$\bar{S} = 0.5$
0	0.1362	0.1302	0.0661	0.0593	0.2612	0.2404
0.05	0.1433	0.1350	0.0692	0.0630	0.2762	0.2545
0.1	0.1499	0.1423	0.0731	0.0651	0.2895	0.2675

Table 3: Normalized resonance frequencies corresponding to harmonic ($\bar{\omega}_0$), subharmonic, and superharmonic excitation regimes for different values of surface tension $\bar{\tau}_s$, for both without prestress ($\bar{S} = 0$) and prestressed ($\bar{S} = 0.5$) configurations.

Surface Elasticity ($\bar{E}_s$) ↓	Normalized Harmonic Resonance Frequency ($\bar{\omega}_0$)		Normalized Subharmonic Resonance Frequency		Normalized Superharmonic Resonance Frequency	
	$\bar{S} = 0$	$\bar{S} = 0.5$	$\bar{S} = 0$	$\bar{S} = 0.5$	$\bar{S} = 0$	$\bar{S} = 0.5$
0	0.1331	0.1172	0.0669	0.0552	0.2651	0.2239
0.2	0.1433	0.1350	0.0692	0.0630	0.2762	0.2545
0.4	0.1495	0.1468	0.0717	0.0685	0.2873	0.2769

Table 4: Normalized resonance frequencies corresponding to harmonic ($\bar{\omega}_0$), subharmonic, and superharmonic excitation regimes for different values of surface elasticity $\bar{E}_s$, for both without prestress ($\bar{S} = 0$) and prestressed ($\bar{S} = 0.5$) configurations.

the three surface mechanisms, surface elasticity produces the strongest upward shift of the harmonic, subharmonic, and superharmonic frequencies, highlighting its dominant role in governing the nonlinear frequency-response characteristics of miniaturized DEAs. For a fixed set of surface properties, the prestressed configuration exhibits lower resonance frequencies than the corresponding without prestress case, reflecting a prestress-induced reduction in the effective dynamic stiffness. Furthermore, for the DEA without pre-stress, the oscillation amplitude shows a slight increase with increasing $\bar{\gamma}_s$ at a given excitation frequency, whereas for the prestressed configuration the amplitude decreases with increasing surface energy density. Overall, the prestressed actuator exhibits frequency-response characteristics qualitatively similar to those of the un-prestressed actuator, with the primary difference being the vibration amplitude. Therefore, to avoid repetition, the discussion on the nonlinear dynamic response of miniaturized DEAs under AC voltage loading is restricted to the un-prestressed case ($\bar{S} = 0$). For completeness, the corresponding results for the prestressed actuator ($\bar{S} = 0.5$) are provided in Appendix B

To elucidate the nonlinear dynamic characteristics of the miniaturized DEA under AC voltage loading, three representative cases corresponding to the maximum considered values of the surface parameters are examined: (i) surface energy density $\bar{\gamma}_s = 0.1$, (ii) surface tension $\bar{\tau}_s = 0.1$, and (iii) surface elasticity $\bar{E}_s = 0.4$. The corresponding transient responses, phase portraits, and Poincaré sections are analyzed under four excitation regimes, namely harmonic, subharmonic, superharmonic, and near-resonant excitation. In each case, the remaining surface parameters are maintained at the same reference values adopted in the frequency-response analysis shown in Fig. 8.

Figures 9(a - c) present the time histories (left panels) together with the corresponding phase portraits and Poincaré sections (right panels) for the three representative surface-effect cases under primary harmonic excitation for the without prestress case ($\bar{S} = 0$). The excitation frequencies are selected from the corresponding primary resonance branches and are taken as $\bar{\omega} = 0.1471$ for the surface energy density case, $\bar{\omega} = 0.1499$ for the surface tension case, and $\bar{\omega} = 0.1495$ for the surface elasticity case,(see Tables 2 - 4). The time-history response (left panels of Fig. 9) exhibits a gradual increase in oscillation amplitude accompanied by envelope modulation, indicative of strong nonlinear resonance effects. Despite this amplification, the response remains bounded over extended time, confirming sustained dynamic stability. The corresponding phase portraits (right panels) show trajectories that expand from an initially compact orbit and evolve into a spiral-like pattern around an inner loop, while remaining confined within a finite region of the phase space. This behavior reflects a departure from periodic motion without the onset of divergence. For the case with $\bar{\gamma}_s = 0.1$, the associated Poincaré map initially forms a closed curve, characteristic of quasi-periodic oscillations, but progressively transitions into a scattered, non-repeating distribution of points, indicating a loss of quasi-periodicity and the emergence of aperiodic yet bounded dynamics under resonant excitation (Zhang & Chen, 2020). For the surface tension and surface elasticity cases, Poincaré maps display a slight spreading of points rather than forming closed invariant curves, indicating that the motion departs from quasi-periodicity and begins to exhibit weakly aperiodic behavior, with signatures of increasing irregularity that may precede transition toward chaotic dynamics (Patra et al., 2024).

At the subharmonic frequencies identified in Tables 2-4 for the aforementioned three representative surface effect cases, the nonlinear dynamic responses presented in Figs. 10 show the miniaturized DEA exhibit dynamically stable quasi-periodic behavior. In contrast to the harmonic-resonance regime, the time histories display

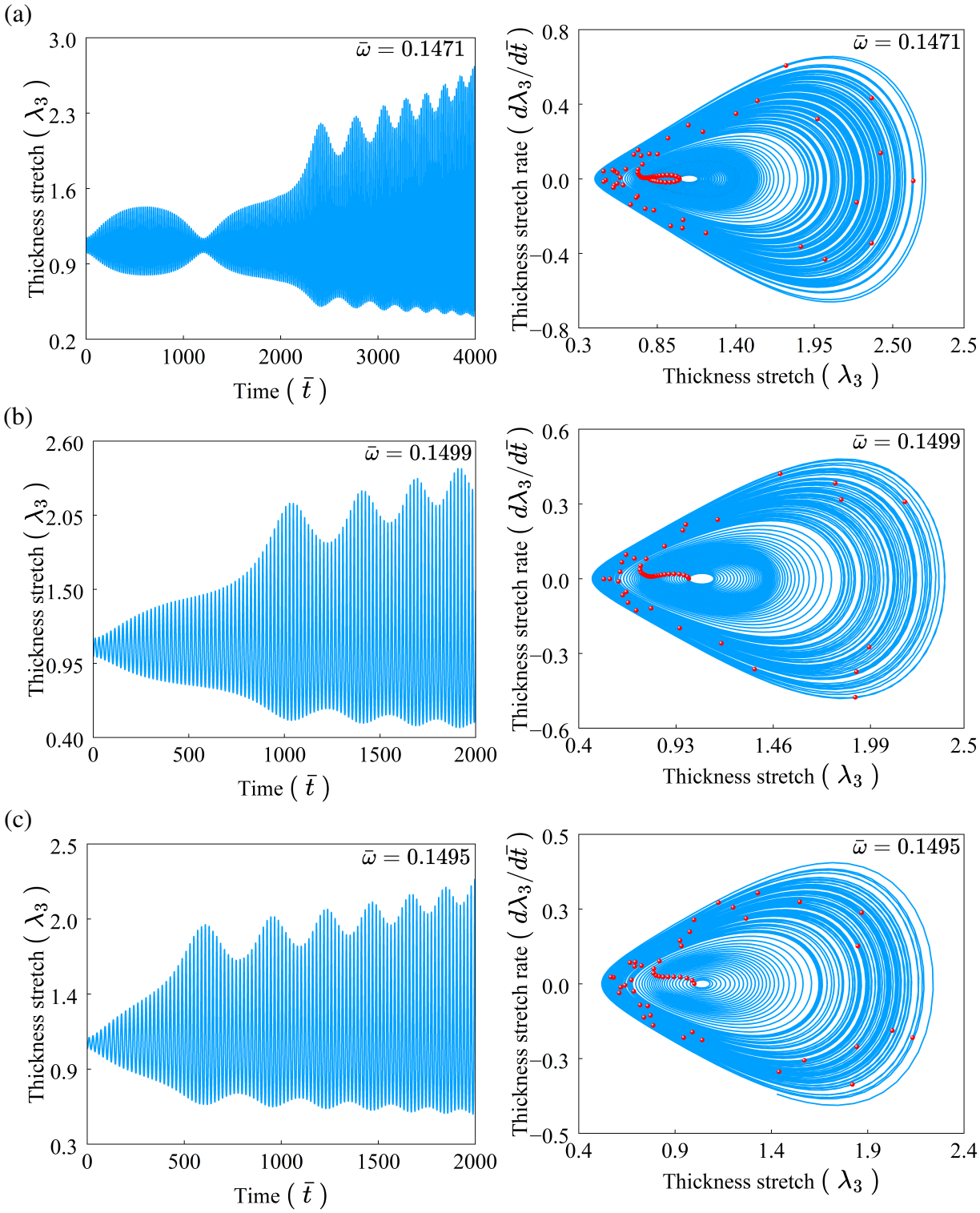

Figure 9: Nonlinear dynamic response of the dielectric elastomer actuator without prestress ($\bar{S} = 0$) under harmonic resonance excitation: the left and right panels show the time histories and the corresponding phase portraits with Poincaré maps, respectively, for (a) $\bar{\gamma}_s = 0.1$, (b) $\bar{\tau}_s = 0.1$, and (c) $\bar{E}_s = 0.4$.

nearly constant-amplitude oscillations with only mild envelope modulation, indicating the absence of significant resonance-driven amplification. The corresponding phase portraits form smooth closed trajectories confined within a finite region of the phase space, thereby confirming regular bounded motion. This behavior is further corrobo-

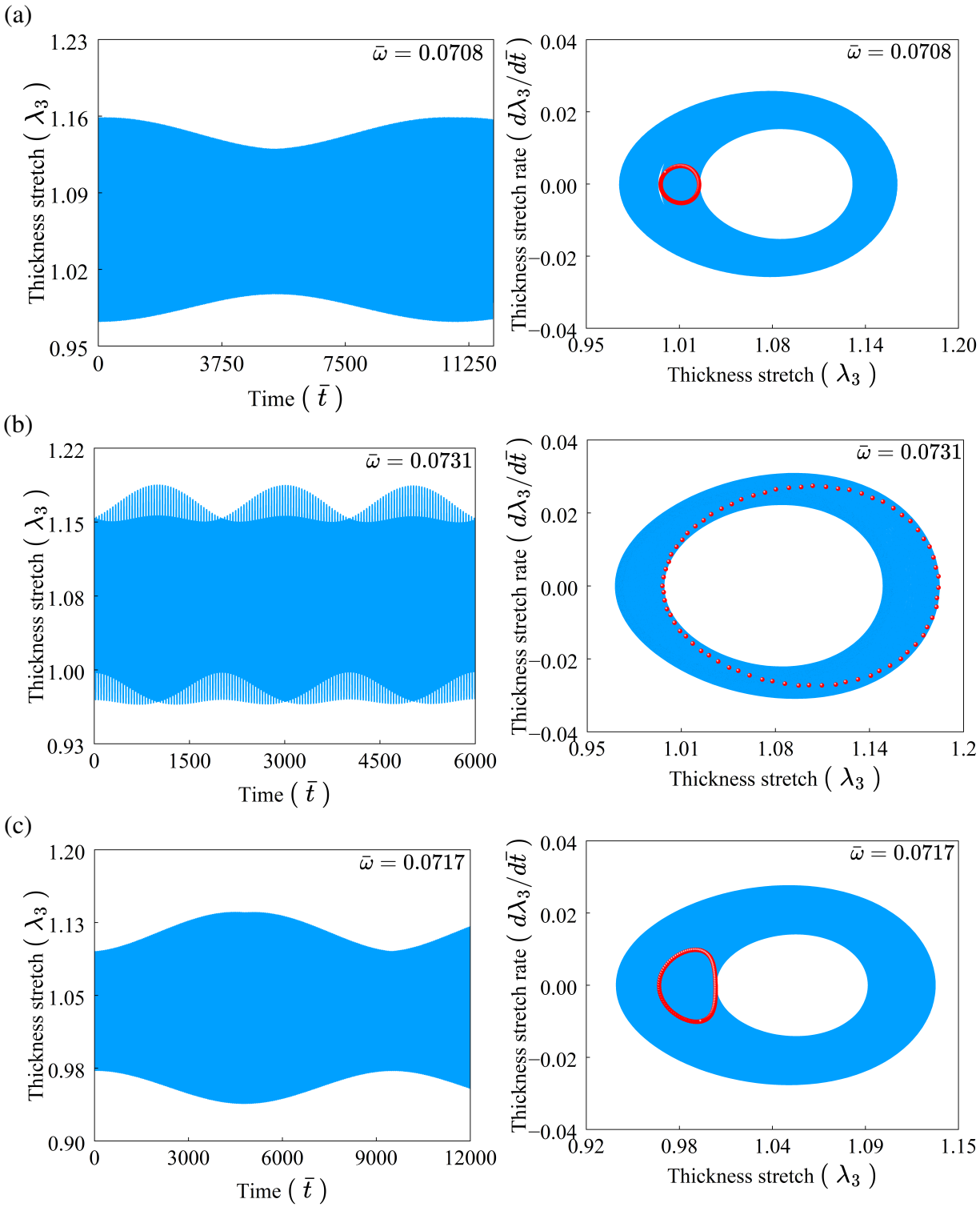

Figure 10: Nonlinear dynamic response of the dielectric elastomer actuator without prestress ($\bar{S} = 0$) under subharmonic resonance excitation. The left and right panels correspond to the thickness-stretch time histories and the associated phase portraits with Poincaré maps, respectively, for (a) $\bar{\gamma}_s = 0.1$, (b) $\bar{\tau}_s = 0.1$, and (c) $\bar{E}_s = 0.4$.

rated by the Poincaré maps, which form closed invariant curves characteristic of quasi-periodic oscillations (Bortot, 2018; Xu et al., 2012; Khurana et al., 2021a). The persistence of invariant tori in the reduced phase space indicates that the nonlinear response remains well ordered under subharmonic excitation. In contrast to the harmonic regime, no signatures of aperiodic or transition to chaotic motion are observed.

Further, as shown in Figs. 11, the nonlinear dynamic response of the miniaturized DEA under superharmonic AC excitation is characterized by bounded yet aperiodic oscillatory motion. The time-history responses exhibit pronounced amplitude modulation with irregular oscillation envelopes, indicating the absence of stable periodic oscillations in the superharmonic regime. This feature is consistently reflected in the phase portraits, where the trajectories expand into finite regions of the phase space without converging to closed orbits, thereby confirming sustained dynamic stability without divergence. The corresponding Poincaré maps do not collapse onto invariant closed curves; instead, they generate non-closed structured point sets, characteristic of bounded aperiodic dynamics (Xiao et al., 2025).

Finally, we examine the voltage-induced beating oscillations of the actuator under excitation frequencies close to the primary harmonic resonance. As depicted in Figs. 12, the time histories exhibit periodic modulation of the oscillation amplitude, arising from the small mismatch between the excitation frequency and the natural frequency of the actuator. This frequency mismatch produces alternating constructive and destructive interference between the interacting oscillatory components, leading to the characteristic envelope modulation observed in the beating response. The corresponding phase portraits form closed and bounded trajectories with finite thickness variations, indicating stable oscillatory motion without divergence. The associated Poincaré maps exhibit closed invariant curves, signifying quasi-periodic dynamics governed by the interaction of closely spaced frequencies.

In the upcoming section, we summarize the key findings of the present study and outline potential directions for future research.

4. Conclusions

In this work, the nonlinear dynamic behavior of an electrically actuated dielectric elastomer actuator incorporating surface effects, namely surface energy density, surface tension, and surface elasticity, has been investigated. The governing equation of motion is derived using the Euler-Lagrange equation for conservative systems and expressed in a dimensionless form to enable a generalized analysis. A neo-Hookean model in-conjunction with ideal dielectric is employed to capture the material response.

The study focuses on two key aspects: (i) the dynamic response and electromechanical instability under DC (Heaviside-type) voltage loading, and (ii) the nonlinear dynamic response under harmonic (AC) excitation. Under DC loading, the time-domain responses and corresponding phase-space characteristics indicate that all three surface parameters introduce a stabilizing influence by suppressing excessive deformation and limiting the growth of oscillations. An energy-based formulation is developed to predict the critical voltage and the associated thickness stretch at the onset of dynamic pull-in instability, incorporating the effects of surface parameters. The analytical predictions are corroborated by direct numerical integration of the nonlinear equation of motion, and close

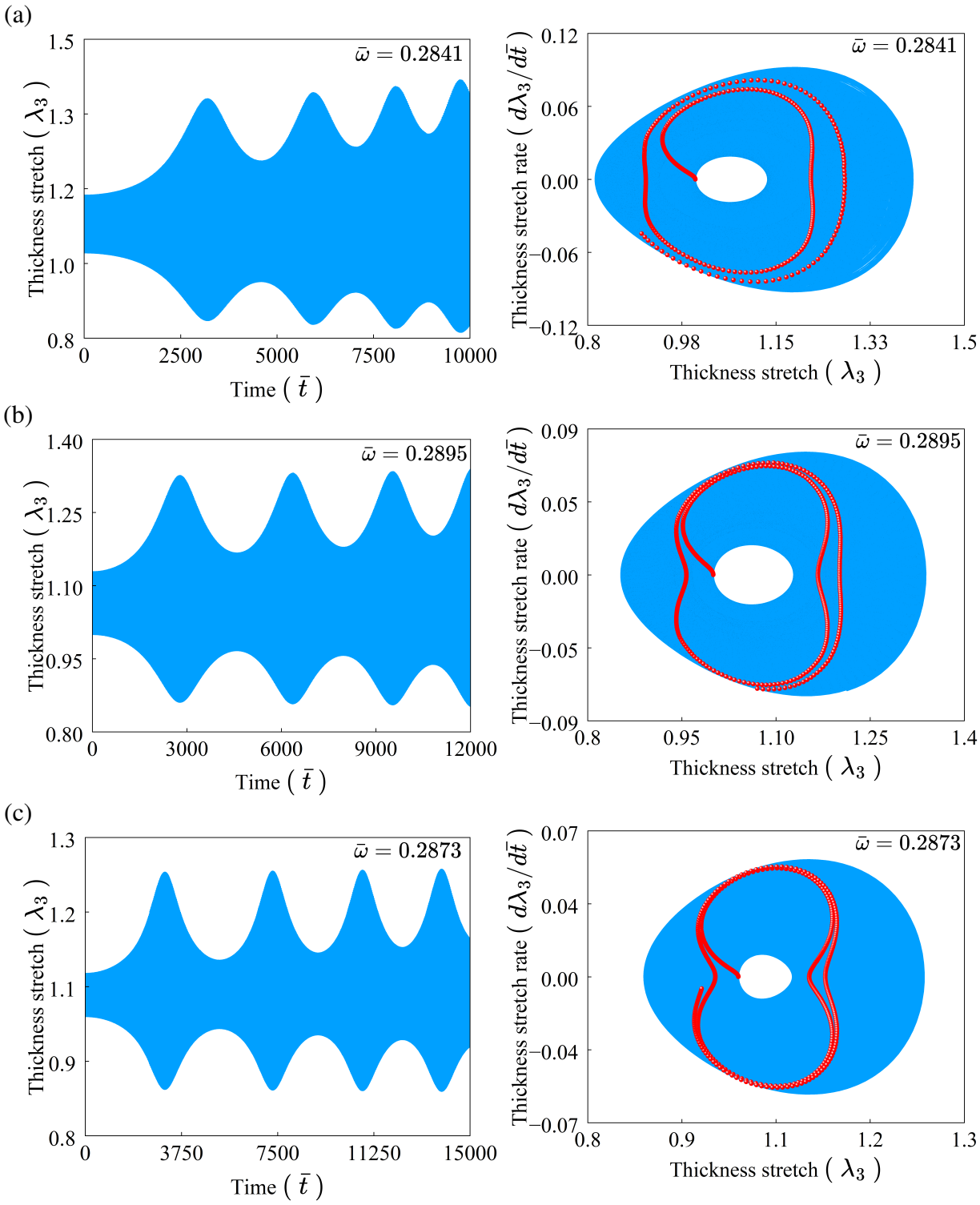

Figure 11: Nonlinear dynamic response of the dielectric elastomer actuator without prestress ($\bar{S} = 0$) under superharmonic resonance excitation. The left and right panels correspond to the thickness-stretch time histories and the associated phase portraits with Poincaré sections, respectively, for (a) $\bar{\gamma}_s = 0.1$, (b) $\bar{\tau}_s = 0.1$, and (c) $\bar{E}_s = 0.4$.

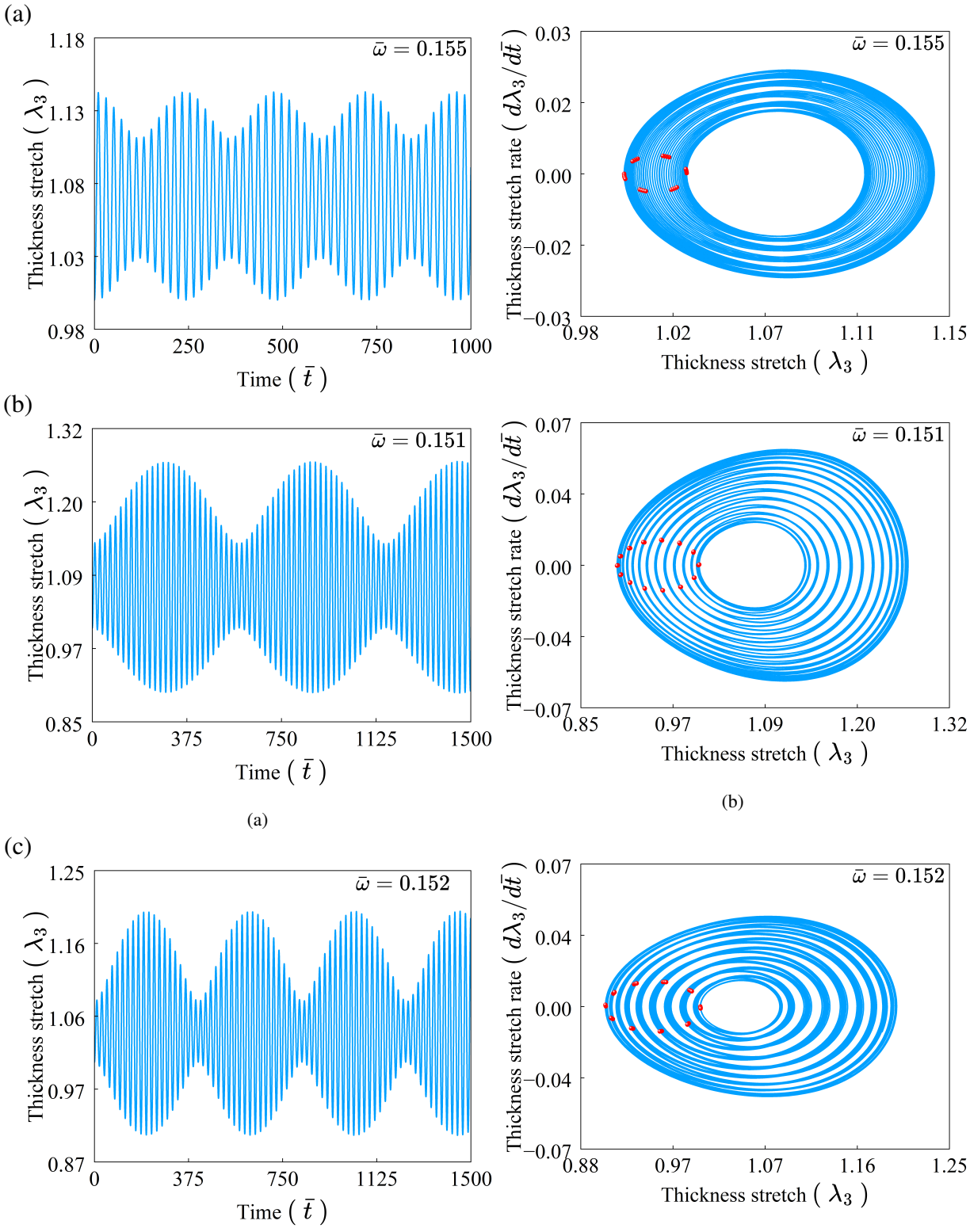

Figure 12: Nonlinear dynamic response of the dielectric elastomer actuator without prestress ($\bar{S} = 0$) under near-resonant excitation. The left and right panels correspond to the thickness-stretch time histories and the associated phase portraits with Poincaré sections, respectively, for (a) $\bar{\gamma}_s = 0.1$, (b) $\bar{\tau}_s = 0.1$, and (c) $\bar{E}_s = 0.4$.

agreement is observed between the two approaches. The results further show that instability persists for surface energy density and surface tension within the considered parameter range, whereas surface elasticity exhibits a stabilizing threshold, beyond which the system remains stable (i.e., $\bar{E}_s > 0.029$), highlighting its pronounced role in enhancing actuator stability.

Under harmonic/AC voltage excitation, the frequency-response analysis demonstrates that increasing $\bar{\gamma}_s$, $\bar{\tau}_s$, and $\bar{E}_s$ leads to a consistent shift of resonance frequencies toward higher values, indicating an increase in the effective stiffness of the actuator. While surface energy density and surface tension tend to slightly increase the oscillation amplitude, surface elasticity reduces the amplitude despite increasing the resonance frequency. Pre-stress lowers the resonance frequencies and results in more compact phase-space trajectories, although its relative influence diminishes at higher surface stiffness.

The nonlinear dynamic analysis reveals distinct response regimes. At harmonic resonance, the actuator exhibits bounded but weakly aperiodic oscillations characterized by non-closed phase trajectories and dispersed Poincaré sections. In the subharmonic regime, the response remains stable and quasi-periodic, with closed phase trajectories and invariant Poincaré curves. Under superharmonic excitation, the system displays bounded aperiodic behavior with distorted phase-space trajectories and non-closed Poincaré structures. In contrast, near-resonant excitation produces amplitude-modulated (beating) responses due to slight detuning, with quasi-periodic characteristics in phase space. In all cases, the responses remain bounded, indicating overall dynamic stability.

In conclusion, the present study demonstrates that surface effects play a critical role in governing both the instability thresholds and nonlinear dynamic behavior of miniaturized DEAs. The proposed modeling framework and findings provide useful guidelines for the design and optimization of soft electroactive actuators, particularly in applications where surface phenomena are significant.

As potential future work, the present dynamic framework can be extended to incorporate viscoelastic constitutive behavior and damping effects (Chiang Foo et al., 2012; Hossain et al., 2012), together with deformation-dependent permittivity, electrostriction, and polarization saturation effects (Jiménez & McMeeking, 2013; Saxena et al., 2014; Pelrine et al., 1998; Gei et al., 2014; Liu et al., 2015). Furthermore, experimental investigations would be necessary to validate the influence of surface effects on the nonlinear dynamic response and pull-in instability characteristics predicted by the present theoretical framework.

Acknowledgment

Authors are grateful to the anonymous reviewers for their insightful comments, which have significantly improved the quality of this manuscript. This work has been carried out as part of the doctoral research of Mr. Akhil Pratap Singh under the supervision of Dr. Atul Kumar Sharma and Dr. Gal Shmuel. A.P.S. acknowledges fellowship support from the Ministry of Education (MoE), Government of India.

Appendix A. Verification of the dynamic model

To verify the dynamic model reported in Section 2.2, we compare the predicted transient response with the

classical dynamic model of dielectric elastomer actuators reported by Joglekar (2014). When all surface parameters, namely the surface energy density $\bar{\gamma}_s$, surface tension $\bar{\tau}_s$, and surface elasticity $\bar{E}_s$, are set to zero, the present formulation (Eq. 15) reduces to the classical dynamic model for ideal dielectric elastomer actuators (Joglekar, 2014; Xu et al., 2012).

For this limiting case, the time-history response under DC voltage loading predicted by the present model is compared with the results reported in Joglekar (2014). The simulation is performed using the following parameters: $H = 2$ mm, $L = 10$ mm, $\mu = 67.1$ kPa, $\rho = 1200$ kg/m^3, $\varepsilon = 6.198 \times 10^{-11}$ F/m, $\bar{\phi} = 0.5$, and $\bar{S} = 0$. The comparison (Fig. A.1) demonstrates excellent agreement between the present predictions and the results reported in Joglekar (2014), thereby verifying the proposed formulation and confirming the generalized nature and reliability of the present dynamic model.

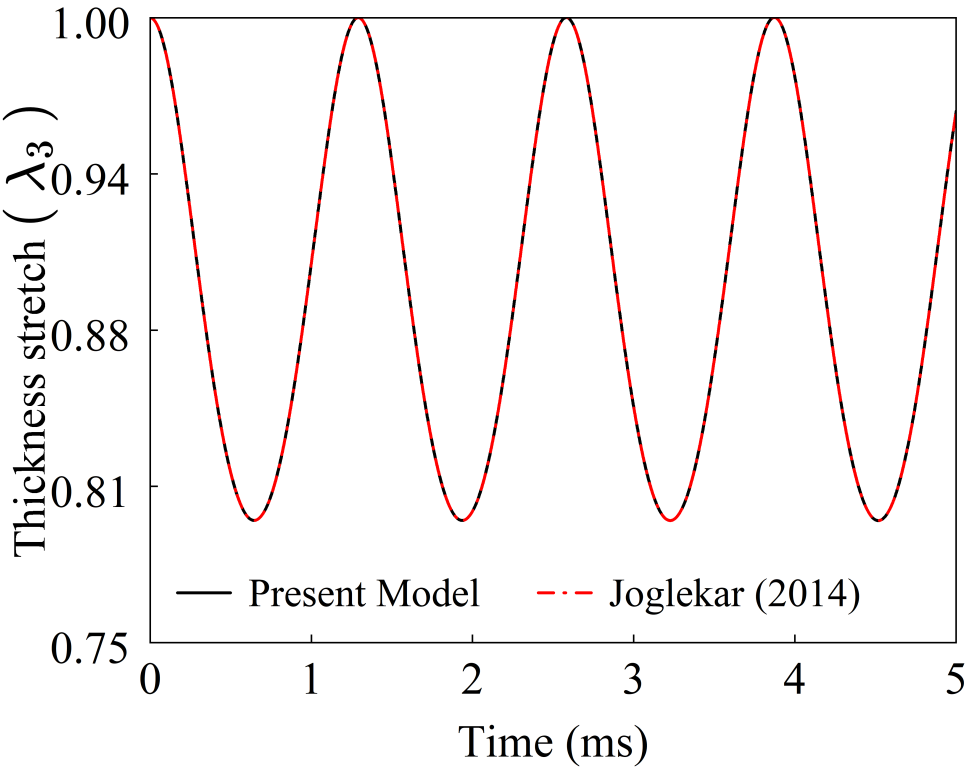

Figure A.1: Verification of the present dynamic model through comparison of the transient response of a dielectric elastomer actuator under DC voltage loading for the limiting case of zero surface effects ($\bar{\gamma}_s = \bar{\tau}_s = \bar{E}_s = 0$) and $\bar{\phi} = 0.5$. The solid line represents the predictions of the present model, while the dashed line corresponds to the results reported by Joglekar (2014).

Appendix B. Dynamic response of the actuator with prestress under harmonic (AC) voltage excitation

Here, the nonlinear dynamic responses of the prestressed miniaturized DEA ($\bar{S} = 0.5$) are presented for the three representative surface-effect cases considered in Section 3.2, under harmonic, subharmonic, superharmonic, and near-resonant excitation conditions.

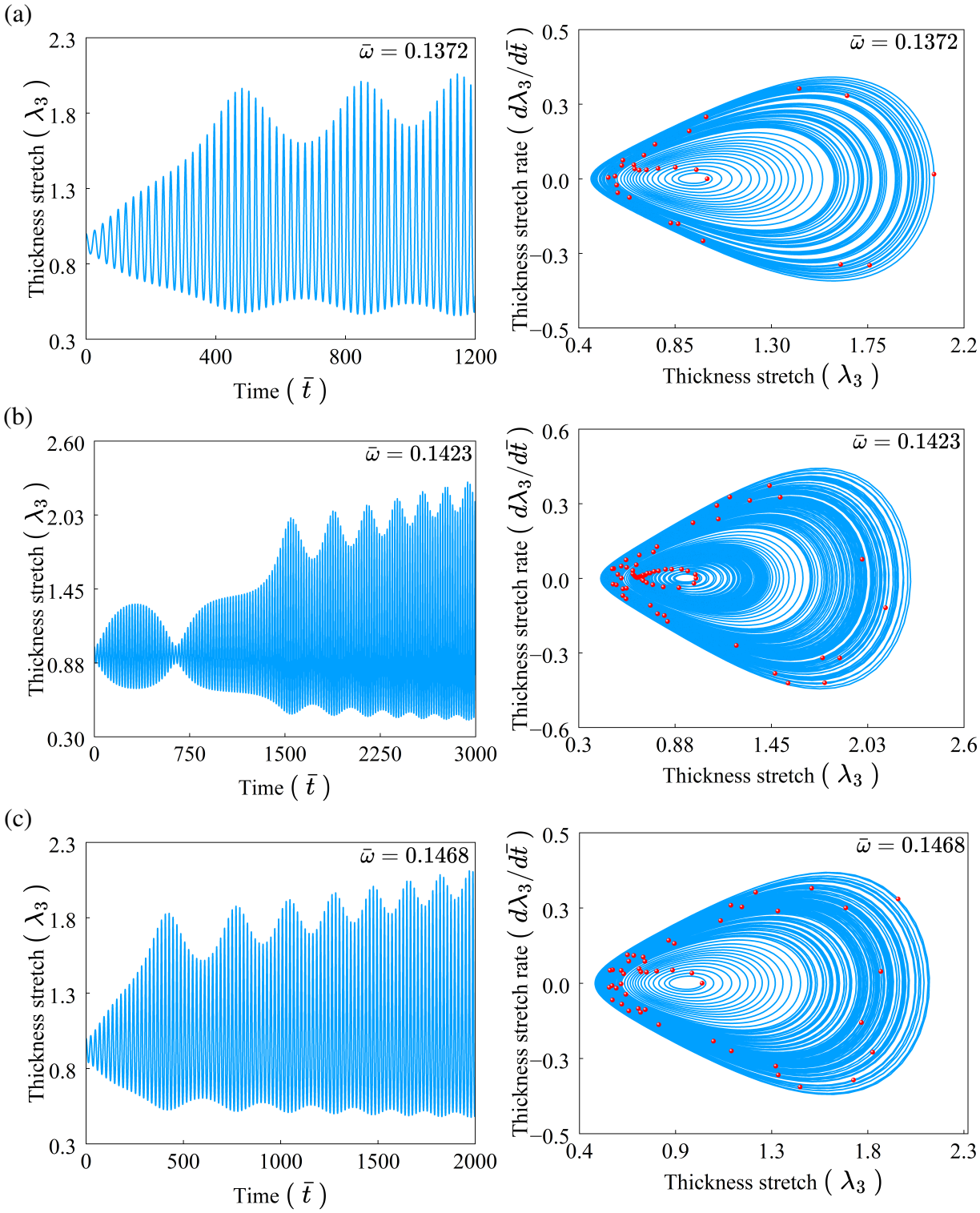

Figure B.1: Nonlinear dynamic response of the dielectric elastomer actuator with prestress ($\bar{S} = 0.5$) under harmonic resonance excitation: the left and right panels show the time histories and the corresponding phase portraits with Poincaré maps, respectively, for (a) $\bar{\gamma}_s = 0.1$, (b) $\bar{\tau}_s = 0.1$, and (c) $\bar{E}_s = 0.4$.

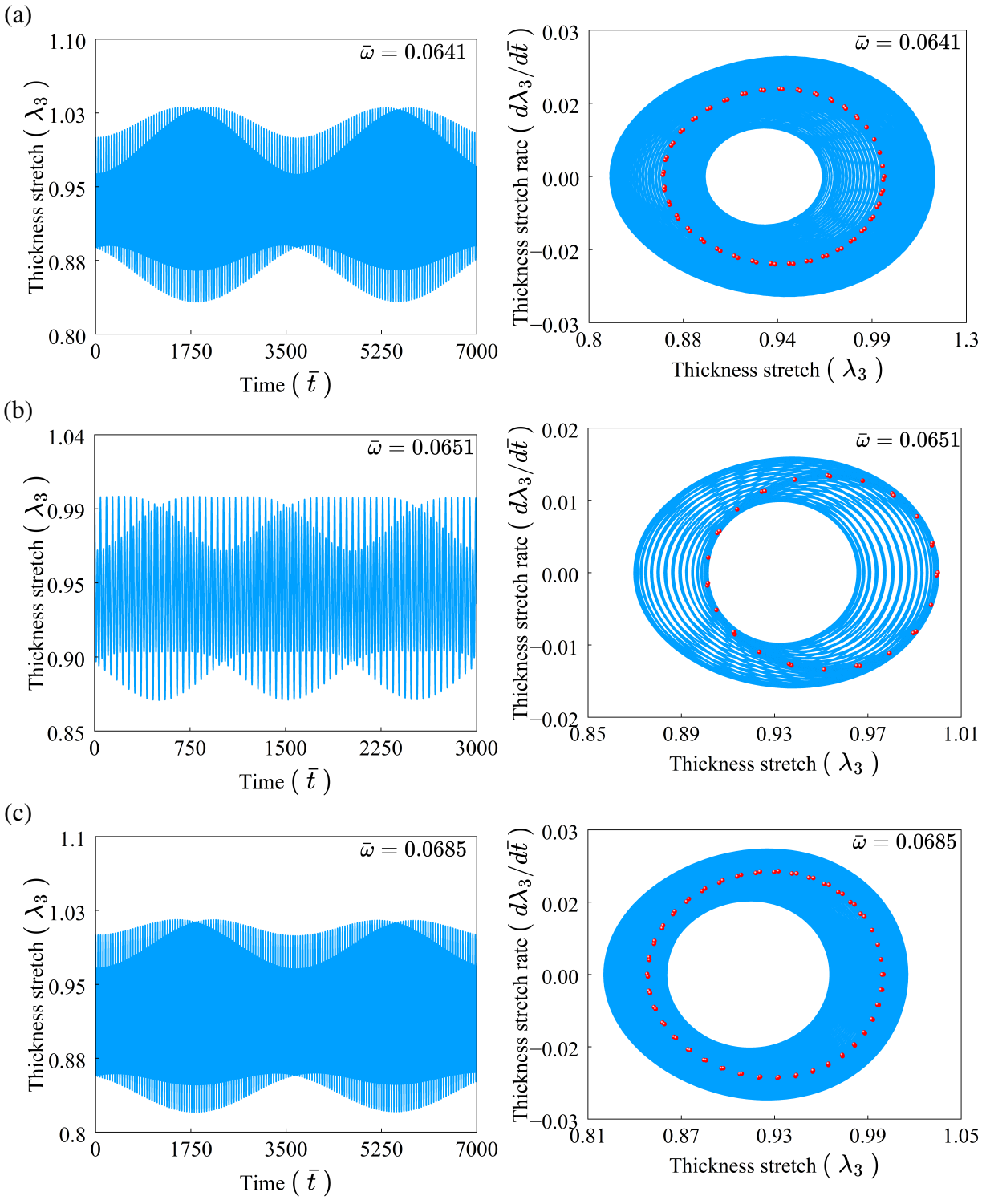

Figure B.2: Nonlinear dynamic response of the dielectric elastomer actuator with prestress ($\bar{S} = 0.5$) under subharmonic resonance excitation. The left and right panels correspond to the thickness-stretch time histories and the associated phase portraits with Poincaré maps, respectively, for (a) $\bar{\gamma}_s = 0.1$, (b) $\bar{\tau}_s = 0.1$, and (c) $\bar{E}_s = 0.4$.

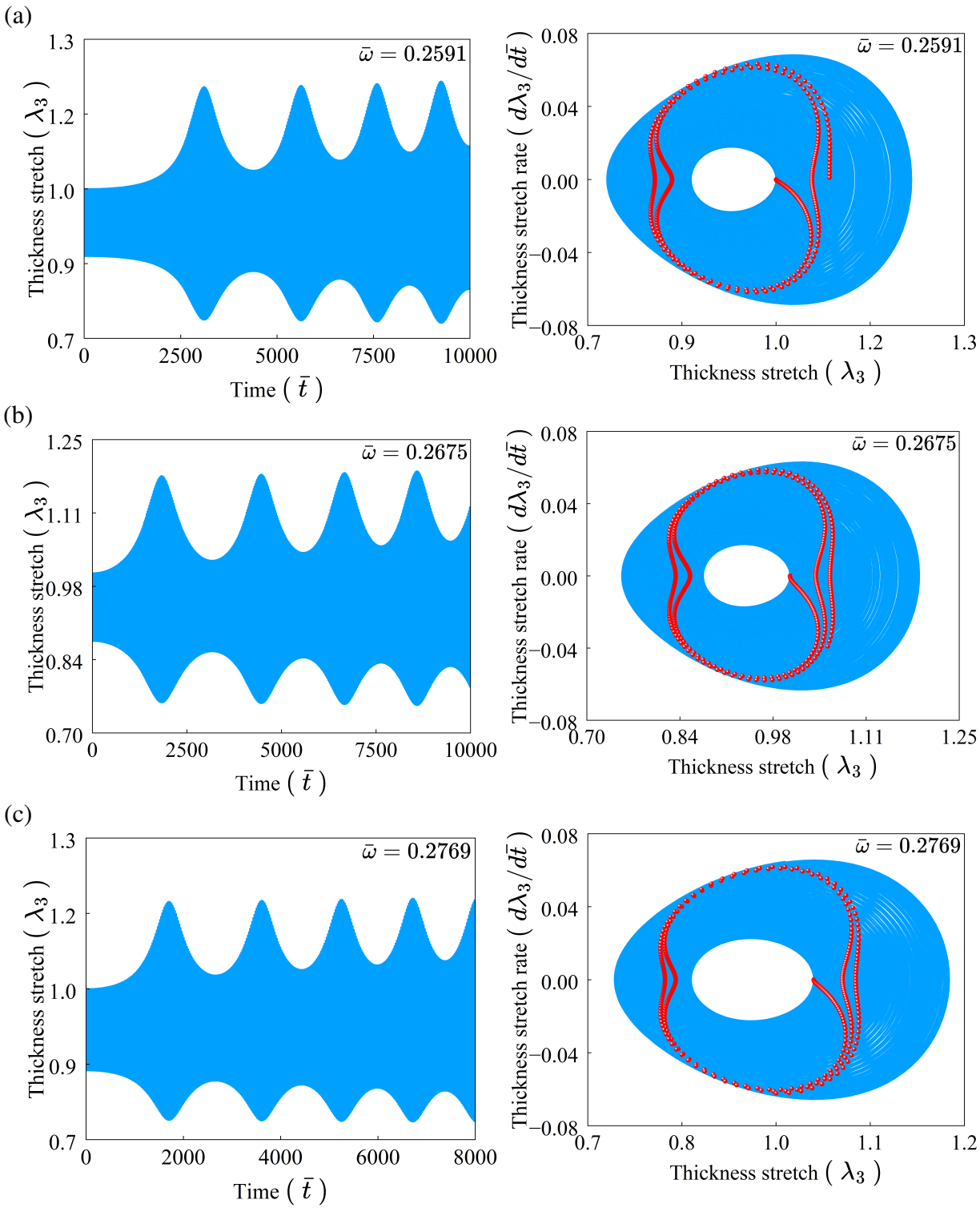

Figure B.3: Nonlinear dynamic response of the dielectric elastomer actuator with prestress ($\bar{S} = 0.5$) under superharmonic resonance excitation. The left and right panels correspond to the thickness-stretch time histories and the associated phase portraits with Poincaré sections, respectively, for (a) $\bar{\gamma}_s = 0.1$, (b) $\bar{\tau}_s = 0.1$, and (c) $\bar{E}_s = 0.4$.

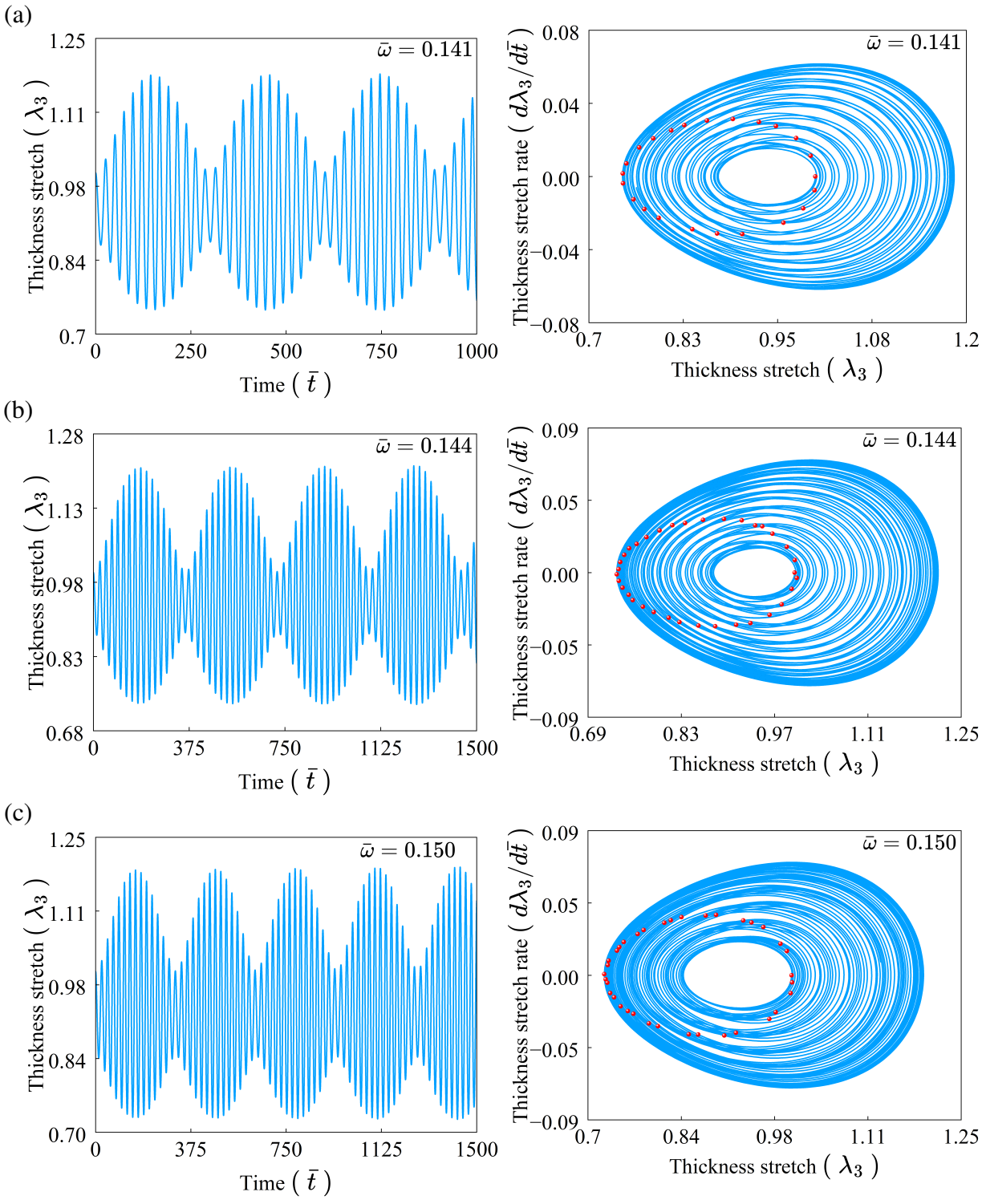

Figure B.4: Nonlinear dynamic response of the dielectric elastomer actuator with prestress ($\bar{S} = 0.5$) under near-resonant excitation. The left and right panels correspond to the thickness-stretch time histories and the associated phase portraits with Poincaré sections, respectively, for (a) $\bar{\gamma}_s = 0.1$, (b) $\bar{\tau}_s = 0.1$, and (c) $\bar{E}_s = 0.4$.

References

Alibakhshi, A., Chen, W., & Destrade, M. (2023). Nonlinear vibration and stability of a dielectric elastomer balloon based on a strain-stiffening model. *Journal of Elasticity*, *153*, 533–48.

Alibakhshi, A., Dastjerdi, S., Fantuzzi, N., & Rahmanian, S. (2022). Nonlinear free and forced vibrations of a fiber-reinforced dielectric elastomer-based microbeam. *International Journal of Non-Linear Mechanics*, *144*, 104092.

Alibakhshi, A., & Heidari, H. (2020). Nonlinear dynamics of dielectric elastomer balloons based on the gent-gent hyperelastic model. *European Journal of Mechanics-A/Solids*, *82*, 103986.

Asgari, M., & Majidi, M. (2025). *Advances in Dielectric Elastomer Composites: A Nonlinear Elasticity Framework*. CRC Press.

Benouhiba, A., Holzer, S., Konstantinidi, S., Civet, Y., & Perriard, Y. (2025). The elastic frontier: dielectric elastomer actuators in healthcare technology. *Smart Materials and Structures*, *34*, 033001.

Bortot, E. (2018). Nonlinear dynamic response of soft thick-walled electro-active tubes. *Smart Materials and Structures*, *27*, 105025.

Bortot, E., & Shmuel, G. (2017). Tuning sound with soft dielectrics. *Smart Materials and Structures*, *26*, 045028.

Cakmak, E., Fang, X., Yildiz, O., Bradford, P. D., & Ghosh, T. K. (2015). Carbon nanotube sheet electrodes for anisotropic actuation of dielectric elastomers. *Carbon*, *89*, 113–20.

Cao, C., Burgess, S. C., & Conn, A. T. (2019a). Toward a dielectric elastomer resonator driven flapping wing micro air vehicle. *Frontiers Robotics AI*, *6*.

Cao, C., Hill, T. L., & Conn, A. T. (2019b). On the nonlinear dynamics of a circular dielectric elastomer oscillator. *Smart Materials and Structures*, *28*, 075020.

Carpi, F., De Rossi, D., Kornbluh, R., Pelrine, R. E., & Sommer-Larsen, P. (2011). *Dielectric elastomers as electromechanical transducers: Fundamentals, materials, devices, models and applications of an emerging electroactive polymer technology*. Elsevier.

Carpi, F., & Rossi, D. D. (2005). Improvement of electromechanical actuating performances of a silicone dielectric elastomer by dispersion of titanium dioxide powder. *IEEE Transactions on Dielectrics and Electrical Insulation*, *12*, 835–43.

Chen, J., Qu, W., Ye, C., Zhao, Z., & Wang, H. (2024). Nonlinear vibration and dynamic stability of dielectric sandwich micro-beams. *International Journal of Mechanical Sciences*, *262*, 108738.

Chen, X., Wang, S., & Yue, Z. (2022). Gurtin and murdoch's surface effect on the elastic behavior of an elastic half space subjected to body forces. *Engineering Analysis with Boundary Elements*, *138*, 118–32.

Chiang Foo, C., Cai, S., Jin Adrian Koh, S., Bauer, S., & Suo, Z. (2012). Model of dissipative dielectric elastomers. *Journal of Applied Physics*, *111*.

Cooley, C. G., & Lowe, R. L. (2023). Nonlinear vibration of dielectric elastomer membranes with axial inertia effects. *International Journal of Mechanical Sciences*, *248*, 108205.

Dai, H., Zou, J., & Wang, L. (2016). Effect of initial stretch ratio on the electromechanical responses of dielectric

elastomer actuators. *Applied Physics A*, *122*, 507.

Dai, H.-l., & Wang, L. (2015). Nonlinear oscillations of a dielectric elastomer membrane subjected to in-plane stretching. *Nonlinear Dynamics*, *82*, 1709–19.

Dorfmann, L., & Ogden, R. W. (2019). Instabilities of soft dielectrics. *Philosophical Transactions of the Royal Society A: Mathematical, Physical and Engineering Sciences*, *377*, 20180077.

Du, F., Lv, P., Li, H., Wang, J., & Shao, L.-H. (2024). A theoretical model to determine solid surface tension through droplet on film configuration and experimental verification. *Journal of the Mechanics and Physics of Solids*, *183*, 105504.

Duduta, M., Wood, R. J., & Clarke, D. R. (2016). Multilayer dielectric elastomers for fast, programmable actuation without prestretch. *Adv. Mater*, *28*, 8058–63.

Eom, S. I., Miyata, K., Asai, K., Kim, J.-W., & Yoshida, K. (2017). Proposal of a peristaltic micropump using dielectric elastomer actuators fabricated by mems technology. In *Electroactive Polymer Actuators and Devices (EAPAD) 2017* (pp. 281–6). SPIE volume 10163.

Fox, C. (1987). *An introduction to the calculus of variations*. Courier Corporation.

Gei, M., Colonnelli, S., & Springhetti, R. (2014). The role of electrostriction on the stability of dielectric elastomer actuators. *International Journal of Solids and Structures*, *51*, 848–60.

Getz, R., Kochmann, D. M., & Shmuel, G. (2017). Voltage-controlled complete stopbands in two-dimensional soft dielectrics. *International Journal of Solids and Structures*, *113*, 24–36.

Ghazali, F. A. M., Mah, C. K., AbuZaiter, A., Chee, P. S., & Ali, M. S. M. (2017). Soft dielectric elastomer actuator micropump. *Sensors and Actuators A: Physical*, *263*, 276–84.

Ghevondyan, M., Davtyan, M., & Aghayan, M. (2025). Dielectric elastomer actuators: Medical applications review. *Discover Materials*, *5*, 43.

Godaba, H., Zhang, Z.-Q., Gupta, U., Foo, C. C., & Zhu, J. (2017). Dynamic pattern of wrinkles in a dielectric elastomer. *Soft matter*, *13*, 2942–51.

Godaba, H., Zhang, Z.-Q., Gupta, U., Foo, C. C., & Zhu, J. (2019). Instabilities in dielectric elastomers: buckling, wrinkling, and crumpling. *Soft Matter*, *15*, 7137–44.

Guo, Y., Li, L., Zhang, D., & Liao, W.-H. (2025). Dynamic modeling and analysis for dielectric elastomer tube actuators. *International Journal of Mechanical Sciences*, *288*, 109994.

Guo, Y., Liu, L., Liu, Y., & Leng, J. (2021). Review of dielectric elastomer actuators and their applications in soft robots. *Advanced Intelligent Systems*, *3*, 2000282.

Gurjar, K. V. S., Sadangi, A. S., Kumar, A., Ahmad, D., Patra, K., Collins, I., Hossain, M., Ajaj, R. M., & Zweiri, Y. (2025). Dielectric elastomer generators: recent advances in materials, electronic circuits, and prototype developments. *Advanced Energy and Sustainability Research*, *6*, 2400221.

Hajiesmaili, E., & Clarke, D. R. (2021). Dielectric elastomer actuators. *Journal of Applied Physics*, *129*.

He, J., Chen, Z., Xiao, Y., Cao, X., Mao, J., Zhao, J., Gao, X., Li, T., & Luo, Y. (2022). Intrinsically anisotropic dielectric elastomer fiber actuators. *ACS Materials Letters*, *4*, 472–9.

He, J., & Park, H. S. (2018). A methodology for modeling surface effects on stiff and soft solids. *Computational*

Mechanics, *61*, 687–97.

Hossain, M. (2020). Modelling the curing process in particle-filled electro-active polymers with a dispersion anisotropy. *Continuum Mechanics and Thermodynamics*, *32*, 351–67.

Hossain, M., Vu, D. K., & Steinmann, P. (2012). Experimental study and numerical modelling of vhb 4910 polymer. *Computational Materials Science*, *59*, 65–74.

Hu, P., Albuquerque, F. B., Madsen, J., & Skov, A. L. (2022). Highly stretchable silicone elastomer applied in soft actuators. *Macromolecular Rapid Communications*, *43*, 2100732.

Huang, C., Zhang, Q., DeBotton, G., & Bhattacharya, K. (2004). All-organic dielectric-percolative three-component composite materials with high electromechanical response. *Applied Physics Letters*, *84*, 4391–3.

Huang, J., Lu, T., Zhu, J., Clarke, D. R., & Suo, Z. (2012). Large, uni-directional actuation in dielectric elastomers achieved by fiber stiffening. *Applied physics letters*, *100*.

Huang, S. Q., & Feng, X. Q. (2008). Spinodal surface instability of soft elastic thin films. *Acta Mechanica Sinica*, *24*, 289–96.

Imamura, H., Kadooka, K., & Taya, M. (2017). A variable stiffness dielectric elastomer actuator based on electrostatic chucking. *Soft matter*, *13*, 3440–8.

Ji, X., Liu, X., Cacucciolo, V., Imboden, M., Civet, Y., El Haitami, A., Cantin, S., Perriard, Y., & Shea, H. (2019). An autonomous untethered fast soft robotic insect driven by low-voltage dielectric elastomer actuators. *Science Robotics*, *4*, eaaz6451.

Jiménez, S. M., & McMeeking, R. M. (2013). Deformation dependent dielectric permittivity and its effect on actuator performance and stability. *International Journal of Non-Linear Mechanics*, *57*, 183–91.

Joglekar, M. M. (2014). An energy-based approach to extract the dynamic instability parameters of dielectric elastomer actuators. *Journal of Applied Mechanics*, *81*, 091010.

Joglekar, M. M. (2015). Dynamic-instability parameters of dielectric elastomer actuators with equal biaxial pre-stress. *AIAA Journal*, *53*, 3129–33.

Kashyap, K., Sharma, A. K., & Joglekar, M. M. (2020). Nonlinear dynamic analysis of aniso-visco-hyperelastic dielectric elastomer actuators. *Smart Materials and Structures*, *29*, 055014.

Khurana, A., Kumar, A., Raut, S. K., Sharma, A. K., & Joglekar, M. M. (2021a). Effect of viscoelasticity on the nonlinear dynamic behavior of dielectric elastomer minimum energy structures. *International Journal of Solids and Structures*, *208*, 141–53.

Khurana, A., Sharma, A. K., & Joglekar, M. M. (2021b). Nonlinear oscillations of electrically driven aniso-visco-hyperelastic dielectric elastomer minimum energy structures. *Nonlinear Dynamics*, *104*, 1991–2013.

Koh, S. J. A., Keplinger, C., Li, T., Bauer, S., & Suo, Z. (2010). Dielectric elastomer generators: How much energy can be converted? *IEEE/ASME Transactions on mechatronics*, *16*, 33–41.

Kornbluh, R., Pelrine, R., Carpi, F., De Rossi, D., & Sommer-Larsen, P. (2008). High-performance acrylic and silicone elastomers. *Dielectric elastomers as electromechanical transducers: Fundamentals, materials, devices, models and applications of an emerging electroactive polymer technology*, (pp. 33–42).

Kumar, A., Khurana, A., Sharma, A. K., & Joglekar, M. (2022). Dynamics of pneumatically coupled visco-

hyperelastic dielectric elastomer actuators: theoretical modeling and experimental investigation. *European Journal of Mechanics-A/Solids*, *95*, 104636.

Lapinski, N., Liu, Z., Yang, S., Hui, C.-Y., & Jagota, A. (2019). A surface with stress, extensional elasticity, and bending stiffness. *Soft Matter*, *15*, 3817–27.

Li, G., Chen, X., Zhou, F., Liang, Y., Xiao, Y., Cao, X., Zhang, Z., Zhang, M., Wu, B., Yin, S. et al. (2021). Self-powered soft robot in the mariana trench. *Nature*, *591*, 66–71.

Li, J., Wang, Z., & Zhou, J. (2024). Mechanics of surface instabilities in soft dielectrics subject to electromechanical loading. *Polymers*, *16*, 3612.

Li, S., Gao, Z., Yang, W., Wang, R., & Zhang, L. (2025a). Recent advances in dielectric elastomer actuator-based soft robots: Classification, applications, and future perspectives. *Gels*, *11*, 844.

Li, X., Wang, S., & Wang, L. (2025b). Surface effects on the electromechanical response of miniaturized dielectric elastomer membranes. *International Journal of Mechanical Sciences*, (p. 110980).

Liguori, P., & Gei, M. (2023). Surface instabilities of soft dielectric elastomers with implementation of electrode stiffness. *Mathematics and Mechanics of Solids*, *28*, 479–500.

Liu, J., Wu, R., & Xia, R. (2014). Surface effects at the nanoscale based on gurtin's theory: a review. *Journal of the Mechanical Behavior of Materials*, *23*, 141–51.

Liu, L., Zhang, Z., Li, J., Li, T., Liu, Y., & Leng, J. (2015). Stability of dielectric elastomer/carbon nanotube composites coupling electrostriction and polarization. *Composites Part B: Engineering*, *78*, 35–41.

Liu, X., Xing, Y., Sun, W., Zhang, Z., Guan, S., & Li, B. (2021). Investigation of the dynamic breakdown of a dielectric elastomer actuator under cyclic voltage excitation. *Frontiers in Robotics and AI*, *8*, 672154.

Lotz, P., Matysek, M., & Schlaak, H. F. (2010). Fabrication and application of miniaturized dielectric elastomer stack actuators. *IEEE/ASME Transactions on mechatronics*, *16*, 58–66.

Lu, L., Li, M., & Wang, S. (2025). Surface effects on buckling instability and large deformation of magneto-active soft beams. *Applied Mathematics and Mechanics*, *46*, 617–32.

Lu, T., Huang, J., Jordi, C., Kovacs, G., Huang, R., Clarke, D. R., & Suo, Z. (2012). Dielectric elastomer actuators under equal-biaxial forces, uniaxial forces, and uniaxial constraint of stiff fibers. *soft matter*, *8*, 6167–73.

Lu, T., Ma, C., & Wang, T. (2020). Mechanics of dielectric elastomer structures: A review. *Extreme Mechanics Letters*, *38*, 100752.

Lu, T., Shi, Z., Shi, Q., & Wang, T. (2016). Bioinspired bicipital muscle with fiber-constrained dielectric elastomer actuator. *Extreme Mechanics Letters*, *6*, 75–81.

Lu, Z., Shrestha, M., & Lau, G.-K. (2017). Electrically tunable and broader-band sound absorption by using micro-perforated dielectric elastomer actuator. *Applied Physics Letters*, *110*.

Ma, G., Wu, X., Chen, L., Tong, X., & Zhao, W. (2020). Characterization and optimization of elastomeric electrodes for dielectric elastomer artificial muscles. *Materials*, *13*, 5542.

Madsen, F. B., Daugaard, A. E., Hvilsted, S., & Skov, A. L. (2016). The current state of silicone-based dielectric elastomer transducers. *Macromolecular rapid communications*, *37*, 378–413.

Masud, M. A. A., Hines, L., Ng, C.-Y., & Hu, J. (2022). Effect of multilayer dielectric elastomer actuator (dea)

construction on performance and breakdown strength. In *Smart Materials, Adaptive Structures and Intelligent Systems* (p. V001T01A013). American Society of Mechanical Engineers volume 86274.

Matysek, M., Lotz, P., Flittner, K., & Schlaak, H. F. (2010). Vibrotactile display for mobile applications based on dielectric elastomer stack actuators. In *Electroactive Polymer Actuators and Devices (EAPAD) 2010* (pp. 83–91). SPIE volume 7642.

McCoul, D., Rosset, S., Schlatter, S., & Shea, H. (2017). Inkjet 3d printing of uv and thermal cure silicone elastomers for dielectric elastomer actuators. *Smart Materials and Structures*, *26*, 125022.

Mills, K., Zhu, X., Takayama, S., & Thouless, M. (2008). The mechanical properties of a surface-modified layer on polydimethylsiloxane. *Journal of materials research*, *23*, 37–48.

Nayfeh, A. H., & Mook, D. T. (2024). *Nonlinear oscillations*. John Wiley & Sons.

Nemani, S. K., Annavarapu, R. K., Mohammadian, B., Raiyan, A., Heil, J., Haque, M. A., Abdelaal, A., & Sojoudi, H. (2018). Surface modification of polymers: methods and applications. *Advanced Materials Interfaces*, *5*, 1801247.

O'Halloran, A., O'Malley, F., & McHugh, P. (2008). A review on dielectric elastomer actuators, technology, applications, and challenges. *Journal of Applied Physics*, *104*, 071101.

Pandey, A. K., Khurana, A., & Sharma, A. K. (2024). Thermo-electro-mechanical effects on nonlinear dynamics of smart dielectric elastomer minimum energy structures. *European Journal of Mechanics-A/Solids*, *105*, 105222.

Pang, X., Li, B., Xia, D., & Jing, S. (2009). Application of dielectric elastomer planar actuators in a micropump chip. In *2009 4th IEEE Conference on Industrial Electronics and Applications* (pp. 1199–202). IEEE.

Patra, A. K., Khurana, A., Kumar, D., & Saxena, P. (2024). Impact of compliant electrodes on the dynamics of electromagnetoactive membranes. *International Journal of Non-Linear Mechanics*, *167*, 104906.

Pelrine, R., Kornbluh, R., Pei, Q., & Joseph, J. (2000). High-speed electrically actuated elastomers with strain greater than 100%. *Science*, *287*, 836–9.

Pelrine, R. E., Kornbluh, R. D., & Joseph, J. P. (1998). Electrostriction of polymer dielectrics with compliant electrodes as a means of actuation. *Sensors and Actuators A: Physical*, *64*, 77–85.

Peng, J., Zhuo, J., Dong, H., Wang, L., Jiang, S., Li, T., & Shi, Y. (2024). Dielectric elastomer actuators with low driving voltages and high mechanical outputs enabled by a scalable ultra-thin film multilayering process. *Advanced Functional Materials*, *34*, 2411801.

Plante, J.-S., & Dubowsky, S. (2006). Large-scale failure modes of dielectric elastomer actuators. *International journal of solids and structures*, *43*, 7727–51.

Ranjan, R. A., Sarangi, S., & Bhattacharyya, R. (2024). Nonlinear dynamics of dielectric actuator: Exploring electrode mechanics. *International Journal of Mechanical Sciences*, *283*, 109755.

Rosales-Cuello, N., Cárcamo, C., Falcón, C., & Palza, H. (2023). Pdms composites with carbon grease as reusable compliant electrodes for applications in artificial muscles based on dielectric elastomer actuators. *Sensors and Actuators A: Physical*, *363*, 114710.

Rosset, S., & Shea, H. R. (2013). Flexible and stretchable electrodes for dielectric elastomer actuators. *Applied Physics A*, *110*, 281–307.

Ru, C. (2010). Simple geometrical explanation of gurtin-murdoch model of surface elasticity with clarification of its related versions. *Science China Physics, Mechanics and Astronomy*, *53*, 536–44.

Saxena, P., Vu, D. K., & Steinmann, P. (2014). On rate-dependent dissipation effects in electro-elasticity. *International Journal of Non-Linear Mechanics*, *62*, 1–11.

Seifi, S., & Park, H. S. (2016). Computational modeling of electro-elasto-capillary phenomena in dielectric elastomers. *International Journal of Solids and Structures*, *87*, 236–44.

Seifi, S., & Park, H. S. (2017). Electro-elastocapillary rayleigh–plateau instability in dielectric elastomer films. *Soft Matter*, *13*, 4305–10.

Seifi, S., Wang, Q., & Park, H. S. (2016). Surface tension effects on surface instabilities of dielectric elastomers. *arXiv preprint arXiv:1611.06419*, .

Sharma, A. K. (2020). Design of a command-shaping scheme for mitigating residual vibrations in dielectric elastomer actuators. *Journal of Applied Mechanics*, *87*, 021007.

Sharma, A. K., Arora, N., & Joglekar, M. M. (2018). Dc dynamic pull-in instability of a dielectric elastomer balloon: an energy-based approach. *Proceedings of the Royal Society A: Mathematical, Physical and Engineering Sciences*, *474*, 20170900.

Sharma, A. K., & Joglekar, M. M. (2018). Effect of anisotropy on the dynamic electromechanical instability of a dielectric elastomer actuator. *Smart Materials and Structures*, *28*, 015006.

Sharma, A. K., & Joglekar, M. M. (2019). Effect of anisotropy on the dynamic electromechanical instability of a dielectric elastomer actuator. *Smart Materials and Structures*, *28*, 015006.

Sharma, A. K., Kosta, M., Shmuel, G., & Amir, O. (2022). Gradient-based topology optimization of soft dielectrics as tunable phononic crystals. *Composite Structures*, *280*, 114846.

Sheng, J., Chen, H., Li, B., & Wang, Y. (2014). Nonlinear dynamic characteristics of a dielectric elastomer membrane undergoing in-plane deformation. *Smart Materials and Structures*, *23*, 045010.

Sheng, J., Chen, H., Liu, L., Zhang, J., Wang, Y., & Jia, S. (2013). Dynamic electromechanical performance of viscoelastic dielectric elastomers. *Journal of Applied Physics*, *114*.

Shi, Y., Askounis, E., Plamthottam, R., Libby, T., Peng, Z., Youssef, K., Pu, J., Pelrine, R., & Pei, Q. (2022). A processable, high-performance dielectric elastomer and multilayering process. *Science*, *377*, 228–32.

Shmuel, G. (2013). Electrostatically tunable band gaps in finitely extensible dielectric elastomer fiber composites. *International Journal of Solids and Structures*, *50*, 680–6.

Shrestha, M., Lau, G., Chin, Y., Teo, E., Khoo, B., & Lu, Z. (2024). A tunable acoustic absorber using reconfigurable dielectric elastomer actuated petals. *Communications Engineering*, *3*, 11.

Singh, A. P., & Sharma, A. K. (2024). Dynamic modeling and analysis of soft dielectric elastomer balloon actuator with polymer chains crosslinks, entanglements and finite extensibility. *International Journal of Applied Mechanics*, *16*, 2450033.

Son, J., Lee, S., Bae, G. Y., Lee, G., Duduta, M., & Cho, K. (2023). Skin-mountable vibrotactile stimulator based on laterally multilayered dielectric elastomer actuators. *Advanced Functional Materials*, *33*, 2213589.

Style, R. W., & Xu, Q. (2018). The mechanical equilibrium of soft solids with surface elasticity. *Soft Matter*, *14*,

4569–76.

Su, Y., Chen, W., & Destrade, M. (2019). Tuning the pull-in instability of soft dielectric elastomers through loading protocols. *International Journal of Non-Linear Mechanics*, *113*, 62–6.

Su, Y., Wu, B., Chen, W., & Lü, C. (2018). Optimizing parameters to achieve giant deformation of an incompressible dielectric elastomeric plate. *Extreme Mechanics Letters*, *22*, 60–8.

Suo, Z. (2010). Theory of dielectric elastomers. *Acta Mechanica Solida Sinica*, *23*, 549–78.

Thomson, G., Yurchenko, D., & Val, D. V. (2018). Dielectric elastomers for energy harvesting. *Energy Harvesting*, (pp. 41–61).

Wang, Q., Liu, M., Wang, Z., Chen, C., & Wu, J. (2021). Large deformation and instability of soft hollow cylinder with surface effects. *Journal of Applied Mechanics*, *88*, 041010.

Wang, Q., & Zhao, X. (2013). Creasing-wrinkling transition in elastomer films under electric fields. *Physical Review E—Statistical, Nonlinear, and Soft Matter Physics*, *88*, 042403.

Wang, R., Zheng, W., Bai, Y., Liang, Y., Wang, Y., & He, J. (2023). Room-temperature self-assembly of poly-(thioctic acid)/silicone dielectric elastomer for highly healable, transparent, electro-sensitive electronic actuator. *Materials Today Nano*, *24*, 100434.

Wang, Y., Ma, X., Jiang, Y., Zang, W., Cao, P., Tian, M., Ning, N., & Zhang, L. (2022). Dielectric elastomer actuators for artificial muscles: A comprehensive review of soft robot explorations. *Resources Chemicals and Materials*, *1*, 308–24.

Wang, Y.-F., Wang, Y.-Z., Wu, B., Chen, W., & Wang, Y.-S. (2020a). Tunable and active phononic crystals and metamaterials. *Applied Mechanics Reviews*, *72*, 040801.

Wang, Z., He, B., Zhou, Y., Shen, R., & Li, G. (2020b). Effects of pre-stretch on the oscillation and stability of dielectric elastomers. *International Journal of Mechanical Sciences*, *185*, 105879.

Wang, Z., Xu, Q., Zhou, Y., Zhu, Z., & He, B. (2024). Modeling of temperature effect on electromechanical properties of dielectric elastomer minimum energy structures. *International Journal of Non-Linear Mechanics*, *159*, 104596.

Weaver Jr, W., Timoshenko, S. P., & Young, D. H. (1991). *Vibration problems in engineering*. John Wiley & Sons.

White, P. J. (2011). *Miniaturization methods for modular robotics: External actuation and dielectric elastomer actuation*. Ph.D. thesis University of Pennsylvania.

Wu, B., Kong, L., Chen, W., Riccobelli, D., & Destrade, M. (2025). Electro-mechanical wrinkling of soft dielectric films bonded to hyperelastic substrates. *Journal of the Mechanics and Physics of Solids*, (p. 106490).

Xiao, Y., Chen, Z., Wang, Y., Lu, H., & Luo, B. (2025). Dynamic behavior of pvc gel actuators: Nonlinear effects of viscoelasticity and electromechanical coupling. *Polymers*, *17*, 633.

Xu, B.-X., Mueller, R., Theis, A., Klassen, M., & Gross, D. (2012). Dynamic analysis of dielectric elastomer actuators. *Applied Physics Letters*, *100*.

Xu, J., Yuan, X. G., Li, Q., & Wang, Y. Q. (2023). Modelling and nonlinear dynamics of dielectric elastomer sandwich cantilever-plate actuators. *European Journal of Mechanics-A/Solids*, *99*, 104943.

Yang, S., & Sharma, P. (2023). A tutorial on the stability and bifurcation analysis of the electromechanical be-

haviour of soft materials. *Applied Mechanics Reviews*, *75*, 044801.

Yin, L.-J., Du, B., Hu, H.-Y., Dong, W.-Z., Zhao, Y., Zhang, Z., Zhao, H., Zhong, S.-L., Yi, C., Qu, L. et al. (2024). A high-response-frequency bimodal network polyacrylate elastomer with ultrahigh power density under low electric field. *Nature Communications*, *15*, 9819.

Yu, X., Lu, Z., Cui, F., Cheng, L., & Cui, Y. (2017). Tunable acoustic metamaterial with an array of resonators actuated by dielectric elastomer. *Extreme Mechanics Letters*, *12*, 37–40.

Zhang, J., & Chen, H. (2020). Voltage-induced beating vibration of a dielectric elastomer membrane. *Nonlinear Dynamics*, *100*, 2225–39.

Zhang, J., Chen, H., & Li, D. (2017). Nonlinear dynamical model of a soft viscoelastic dielectric elastomer. *Physical Review Applied*, *8*, 064016.

Zhang, L., Shi, X., Gu, G., Zou, J., & Liu, J. (2025a). Hyper-viscoelastic dynamic modeling and analysis for soft dielectric elastomer actuators. *Mechanical Systems and Signal Processing*, *241*, 113405.

Zhang, X., Zhao, Z., Wang, Z., Xu, W., Ke, K., Liu, Z., & Yang, W. (2025b). Multilayer dielectric elastomer actuator with enhanced breakdown strength via regulating the layer thickness ratio. *ACS Omega*, .

Zhao, X., & Suo, Z. (2007). Method to analyze electromechanical stability of dielectric elastomers. *Applied Physics Letters*, *91*.

Zhao, X., & Suo, Z. (2010). Theory of dielectric elastomers capable of giant deformation of actuation. *Physical review letters*, *104*, 178302.

Zhao, Z., Chen, Y., Hu, X., Bao, R., Wu, B., & Chen, W. (2023). Vibrations and waves in soft dielectric elastomer structures. *International Journal of Mechanical Sciences*, *239*, 107885.

Zhao, Z., Shuai, C., Gao, Y., Rustighi, E., & Xuan, Y. (2016). An application review of dielectric electroactive polymer actuators in acoustics and vibration control. In *Journal of Physics: Conference Series* (p. 012162). IOP Publishing volume 744.

Zheng, B., Man, X., Andelman, D., & Doi, M. (2021). Enhanced electro-actuation in dielectric elastomers: the nonlinear effect of free ions. *ACS Macro Letters*, *10*, 498–502.

Zhou, F., He, J., Zhang, M., Xiao, Y., Chen, Z., Wong, T.-W., Li, T., Xu, Z., & Luo, Y. (2021). Electromechanical model-based adaptive control of multilayered dielectric elastomer bending actuator. *Journal of Applied Mechanics*, *88*.

Zhu, J. (2015). Instability in nonlinear oscillation of dielectric elastomers. *Journal of Applied Mechanics*, *82*, 061001.

Zhu, J., Cai, S., & Suo, Z. (2010). Resonant behavior of a membrane of a dielectric elastomer. *International Journal of Solids and Structures*, *47*, 3254–62.

Zhu, J., Chen, H., Wu, B., Chen, W., & Balogun, O. (2018). Tunable band gaps and transmission behavior of sh waves with oblique incident angle in periodic dielectric elastomer laminates. *International Journal of Mechanical Sciences*, *146*, 81–90.